Topographic, Geophysical, and Mineralogical Characterization of Geologic Structures Using a Statistical Modeling Approach

By Robert R. McDougal, Anne E. McCafferty, Bruce D. Smith, and Douglas B. Yager

Chapter E13 of
Integrated Investigations of Environmental Effects of Historical Mining in the Animas River Watershed, San Juan County, Colorado
Edited by Stanley E. Church, Paul von Guerard, and Susan E. Finger

Professional Paper 1651

U.S. Department of the Interior
U.S. Geological Survey

Contents

Abstract 647
Introduction 647
    Purpose and Scope 649
Geologic Structures 649
Data Collection and Compilation 649
    Airborne Geophysical Data 651
    Geologic Structural Data 651
    Data Accuracy 651
    Remote Sensing Data 652
Methods 655
    Calculation of Planimetric Orientation of Structures and Geophysical Gradients 655
    Predictive Modeling Methodology 655
    Data Preparation for Predictive Modeling 656
        Topographic Data 656
        Magnetic Data Enhancement 656
        Electrical Resistivity Data 657
        Remote Sensing Data 665
Results and Analysis 665
    Planimetric Orientation of Geologic Structures and Geophysical Gradients 665
    Weights Charts and Predictive Models 665
    Profile Convexity Model 665
    Resistivity Model 667
    Magnetic Models 668
        Magnetic Characteristics of Shallow Geologic Structures 668
        Magnetic Characteristics of Deep Crust Geologic Structures 670
    Mineralogic Models 675
    Model Validation 676
        Model Stability 676
        Comparison of Geophysical and Profile Convexity Profiles to Geologic Cross Sections 676
        Field Verification 683
Conclusions and Discussion 686
References Cited 686

Figures

1. Generalized map of selected geographic and geologic features in the Animas River watershed study area 648
2. Index map of extent of structural, airborne geophysical, and AVIRIS data sets 650
3. Map of mineralized and nonmineralized faults and veins 652
4. AVIRIS mineral map showing acid-generating potential minerals 653
5. AVIRIS mineral map showing acid-neutralizing potential minerals 654
6. Images of shaded relief Digital Elevation Model and derived profile convexity model 656
7. Reduced-to-pole magnetic anomaly map 658

8–11. Maps showing:
8. "High-pass" filtered magnetic anomalies calculated from RTP magnetic data.....659
9. "Low-pass" filtered magnetic anomalies.....660
10. "High-pass" horizontal magnetic gradient anomalies calculated from RTP magnetic data 661
11. "Low-pass" horizontal magnetic gradient anomalies calculated from RTP magnetic data 662
12. Profile illustration of various transformations applied to the Silverton magnetic data 663
13. Map showing 4,310-Hz apparent resistivity data 664
14. Data layer images used to produce masked coverage of faults and veins from AVIRIS vegetation and snow cover mapping.....666
15. Rose diagrams showing planimetric orientation of mapped geologic structure and geophysical gradient trends from airborne geophysical survey 667
16. Graph showing calculated weights of the relationship of structures to topography.....668
17. Map showing profile convexity predictive model of geologic structures.....669
18. Graph showing weights of association of electrical resistivity with mapped structures.....670
19. Map showing electrical resistivity predictive model of geologic structures 671
20. Images showing predictive model of resistivity—location of ground electromagnetic survey in Placer Gulch 672
21. Graphs showing calculated weights of magnetic high-pass filtered data and high-pass filtered horizontal gradient magnitude associations with geologic structure.....673
22. Map showing high-pass horizontal gradient magnitude magnetics predictive model of geologic structures.....674
23. Graph showing calculated weights of geologic structure association with low-pass magnetic horizontal gradient magnitude 675
24. Bar graphs showing calculated weights of geologic structure association with acid-generating potential and acid-neutralizing potential group minerals.....677
25. Graphs showing comparison of predictive models for verification 678
26. High-pass magnetic, 4,310 Hz apparent resistivity, and profile convexity profiles over geologic cross section *A–A'*.....679
27. High-pass magnetic, 4,310 Hz apparent resistivity, and profile convexity profiles over geologic cross section *B–B'*.....680
28. Images showing comparison of profile convexity, resistivity, and magnetic models and maps to a silicified vein in Boulder Gulch.....684
29. Images showing comparison of profile convexity, resistivity, and magnetic models and maps to an altered and eroded zone near the headwaters of South Fork Cement Creek.....685

Tables

1. Numerical comparison of geologically mapped structure locations along profiles *A–A'* (fig. 26) and *B–B'* (fig. 27) to locations of geologic structures predicted by high-pass magnetic, 4,310 Hz resistivity, and profile convexity models 682

Chapter E13
Topographic, Geophysical, and Mineralogical Characterization of Geologic Structures Using a Statistical Modeling Approach

By Robert R. McDougal, Anne E. McCafferty, Bruce D. Smith, and Douglas B. Yager

Abstract

Statistical modeling of geologic structures in the Animas River watershed study area enables definition of geophysical (electromagnetic and magnetic), mineralogical, and topographic attributes, portrayed in charts and maps as probabilities. The modeling shows that faults and veins in the watershed have characteristic signatures within discrete data value ranges for all data layers, as evident by relatively high probabilities. Topographically, structures are characterized by erosionally resistive and likely silicified ridgelines, or appear as eroded incised channels and valleys. Geophysically, the planimetric orientations of structures calculated from the trends of geophysical gradients identify east-west, northerly, and northwesterly trends, which are collinear with trends of mapped geologic structures. Magnetically, the faults and veins are mostly characterized by extremely low magnetizations that are associated with the magnetite-poor mineralogy of the silicic vein material. Although a less typical case, some faults and veins are characterized by moderately high magnetizations. Magnetization boundaries associated with rocks located at depths exceeding 1 kilometer identify surface structures that likely provide connectivity between the topographic surface and deep crust, and revealed buried crustal boundaries not mapped at the surface. Mapped faults and veins are characterized by moderately high electrical resistivities consistent with the silicic mineralogy of the vein material but may also point to silica-rich phases within volcanic rocks in the study area. The mineralogical character of structures in terms of their acid-producing or acid-neutralizing potential suggests no significant association with acid production resulting from the weathering of pyrite. Structures are most likely to occur in propylitically altered areas, and they are therefore associated with rocks with the highest acid-neutralizing potential. In map form, the predictive models show high probabilities that accurately locate many known structures but, more interestingly, map areas devoid of structures. Many of the permissive areas for unmapped structures, however, lie in places of restricted access, limited outcrop, and thick alluvium, soil, or vegetation cover. Our validation methods show that the models can successfully locate known structures and predict the location of previously unknown structures.

The predictive models presented in this study could be considered in remediation planning, or used as an exploration tool for ground-water or mineral resource applications. The methods and approaches employed here can be applied to other watersheds with similar structural and volcanic regimes containing acid-generating historical mines or source rocks.

Introduction

The Animas River watershed study has produced substantial geologic, geochemical, and geophysical data, and related scientific analysis. Mapped geologic structure, digital terrain, airborne magnetic and resistivity data, and remotely sensed mineral mapping are available for most of the watershed area and provide the necessary data for regional to local-scale analysis and investigations. In this study, we use these data sets and derivative products to provide an understanding of how physical parameters relate to and typify mapped geologic structures, specifically, faults, fractures, and mineralized veins. These linear and curvilinear structures are assumed to be positively associated with local, subregional, and regional ground-water flow regimes, particularly in the vicinity of the Eureka graben, caldera margins, and South Silverton mining area (Yager and Bove, this volume, Chapter E1) (fig. 1). In some cases, structures provide pathways for ground-water flow. In contrast, where faults and veins are annealed with quartz, they may act as barriers to flow.

An attempt to describe the mechanics of ground-water flow through bedrock needs to consider the physical characteristics of the bedrock. In this study, it was necessary to define bedrock structural trends, identify the mineralogy within

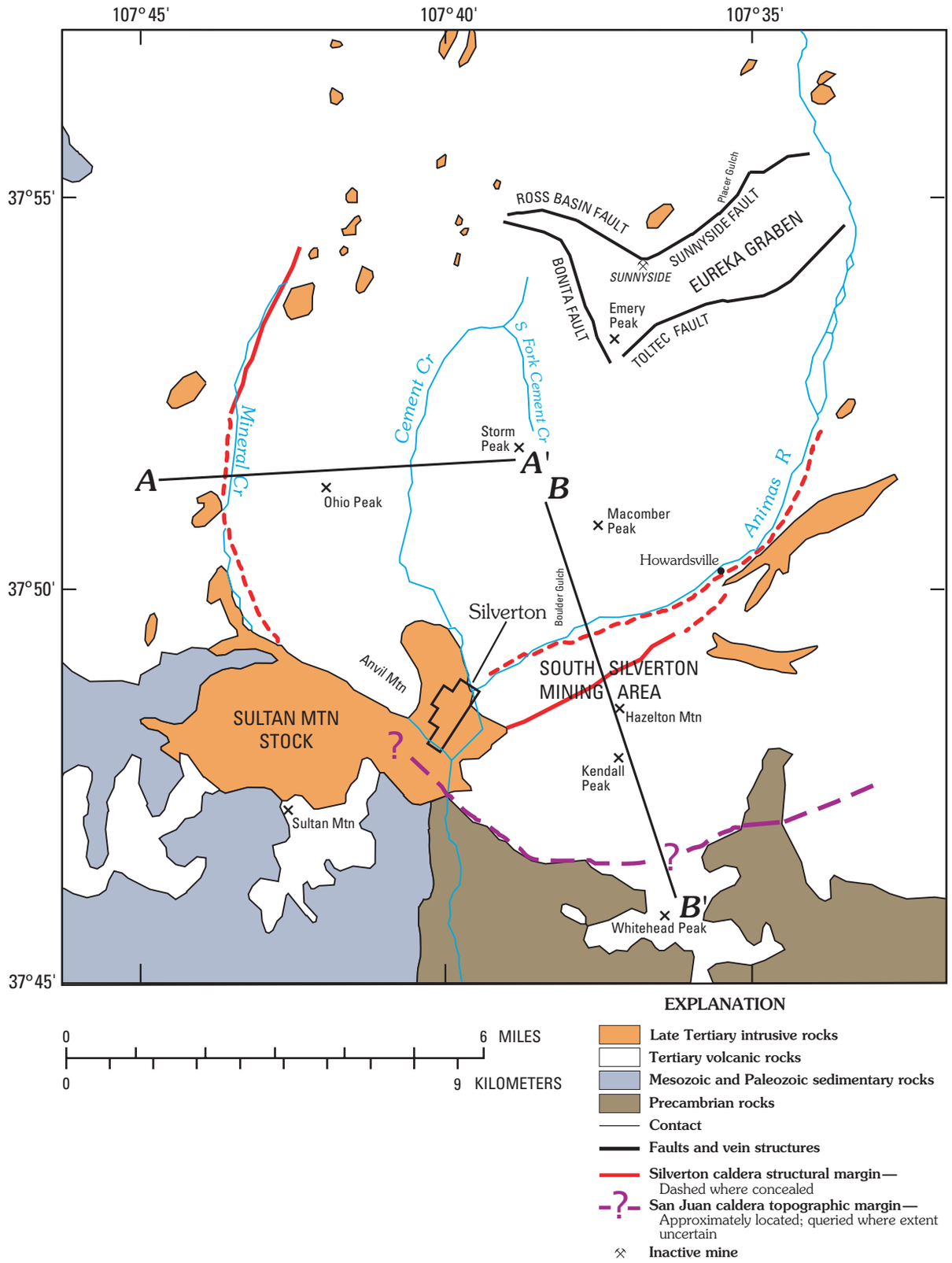

Figure 1. Selected geographic and geologic features in the Animas River watershed study area. Modified from Yager and Bove (2002). Cross sections *A*–*A*' and *B*–*B*' are discussed in a later section and are shown in figures 26 and 27 (p. 679, 680).

structures, understand the geophysical signatures of structures, and finally, determine how structures are geomorphologically expressed in order to differentiate between structures that likely are hydraulically conductive and those that are not. Determining the mineralogical characteristics of structures may provide useful environmental information by differentiating structures that may have increased acid-generating potential and consequently may be associated with increased metal loading to ground and surface water, or alternatively, by identifying structures that are possibly associated with greater acid-neutralizing potential.

In this study, we derived models using statistical methodology to quantify the topographic, geophysical, and mineralogical signatures of mapped mineralized and nonmineralized faults and veins in the watershed. The calculated probabilities describe the association between a structural feature and a data layer, and can be expressed as either positive or negative associations. The analyses should reveal which parameters (topography, electrical resistivity, magnetic signature, or mineralogy) are *least* likely to characterize structural features (negative association), and alternately, which are *most* likely to characterize structural features (positive associations). Results of the calculations quantify characteristics of the geologic structures. Additionally, a series of predictive maps identify areas within the watershed that exhibit characteristics similar to those of the known faults and veins.

The predictive models presented here can identify areas where previously unmapped structures may exist. This information could be considered in remediation planning, or it could be used as an exploration tool for ground-water or mineral resource applications, as it contributes to a more complete understanding of ground-water and surface-water interactions, metal loading to streams, and identification of possible ground-water pathways.

Purpose and Scope

The purpose of this investigation is to define the topographic, geophysical, and mineralogical characteristics of mineralized faults and veins in the study area and to use this information to infer the locations of exposed and buried geologic structures in the watershed. The objectives of the study are to:

- Examine the relationship of geologic structure to topography. Determine the geomorphological characteristics of mapped structure and identify the types of terrain where faults and mineralized veins occur
- Determine the structural trends (planimetric orientation) of mineralized faults and veins, and compare their orientations to those of geophysical gradient trends
- Determine the geophysical (magnetic and electrical resistivity) characteristics of mapped structures
- Using remotely sensed data, determine the environmental effects of mapped structures in terms of their acid-neutralizing or acid-generating potential as indicated by mineral assemblages
- Identify areas where previously unmapped structures may exist based on topographic, geophysical, and mineralogical attributes.

Geologic Structures

For the purposes of this study, the general terms “geologic structure” or “structures” are intended to refer specifically to mineralized and nonmineralized faults and veins. The prominent fault systems and extensive mineralization of faults and veins of the San Juan–Uncompahgre and Silverton calderas are of particular interest in terms of their potential as flow paths for structurally controlled ground water. Faults occur as ring faults associated with the caldera structural margin, as adjacent radial faults, and as faults associated with the Eureka graben. In some areas of the watershed, vein orientation appears to be strongly associated with the degree of mineralization. In the South Silverton mining area (fig. 1), southeast of Silverton, and near the northwestern boundary of the caldera, northwest-trending veins, perpendicular to the structural margin ring faults, are relatively more mineralized. Near the Eureka graben, mineralized structures generally trend to the northeast (approximately 45°) or to the northwest (approximately 270°) (Casadevall and Ohmoto, 1977).

Veins in the study area commonly occur in broad zones that have undergone multiple episodes of mineralization. Such zones in the South Silverton mining area have been described as country rock traversed irregularly by ore-bearing stringers, which can attain a width of about 30 m (Burbank, 1933). The wider veins and bodies of veined and altered rock in the Sunnyside vein system achieve a width of 30 m. Ore stopes in the Sunnyside mine are reported to have been 15 m wide in some places (Burbank and Luedke, 1969). Outcrop vein widths of several meters were observed in several places across the Sunnyside and Ross Basin fault vein systems in Eureka Gulch and across the Toltec fault in Eureka Gulch. Field observations of veins in the study area have aided us in determining the appropriate proximity zone used in the analysis presented here.

Topographically, faults and veins can create zones of erosional weakness, resulting in linear to curvilinear valleys, gullies, and stream channels. Alternatively, where faults and veins are silicified, erosionally resistive linear ridges can form.

Data Collection and Compilation

This section describes the basic data layers and related processing and transformations that we applied as preparation for calculating orientations of structural trends and performing the predictive modeling. The areal extent of each data set used in the analysis is shown in figure 2.

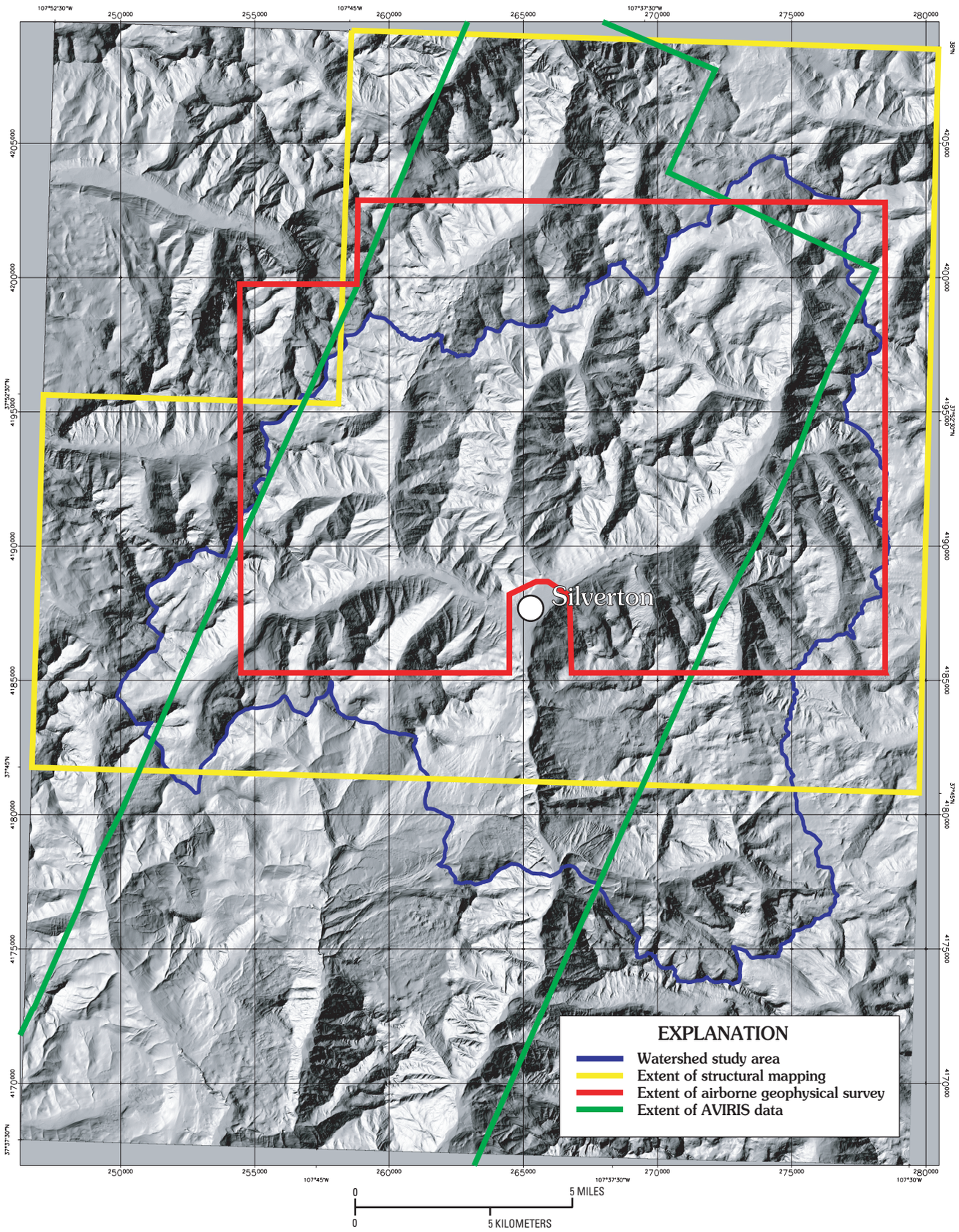

Figure 2. Extent of structural, airborne geophysical, and AVIRIS data sets.

Airborne Geophysical Data

An airborne geophysical survey was flown over the Animas River watershed study area and surrounding region during the fall of 1998. Magnetic and electromagnetic (EM) data were collected along north-south flightlines at a 200 m spacing for the west half of the watershed and at 400 m spacing for the eastern part of the watershed. The electromagnetic field was measured with three frequencies (984, 4,310, and 33,000 Hz) using horizontal coplanar transmitting and receiving coils towed in a capsule container ("bird") that varied in elevation but was generally located at approximately 30 m above the ground surface. The helicopter towed the sensor at higher altitudes where appropriate for safe flying, for example, over power lines, tramlines, and on ascent up steep mountainsides. Accurate measurement of EM fields from a helicopter platform requires that the sensor be positioned at low altitudes. However, due to the extremely rugged topography within the Animas River watershed study area, safe flying dictated that the EM sensor was, at times, out of range for collection of accurate EM data. Data were not collected over populated areas. Areas within the survey where the EM data are inaccurate or absent are mapped as white on the resistivity maps and associated derivative products. The EM data were post-processed to compute values of apparent resistivity (Fraser, 1978).

The total field magnetic sensor was also mounted in the EM bird. Magnetic-field measurements are less affected by altitude variations; therefore, the maps of magnetic data and derivative products have complete coverage within the area covered by the airborne survey. The total field data were post-processed to remove diurnal variations produced by the Earth's magnetic field.

Flightline data for the magnetic and resistivity data were interpolated onto a 40 m interval grid for the western part of the survey and onto an 80 m interval grid for the eastern part of the survey to maintain data resolution for each survey. The grid interval along the north-south flightlines was 3 m. Data for the eastern part of the survey were resampled to a 40 m interval and merged with the west survey grid to create a composite grid. A description of the digital flightline data, grids, and information on other derivative geophysical products from this survey are available in Smith and others (this volume, Chapter E4).

Geologic Structural Data

Structural data were compiled from numerous paper map sources that were originally produced at multiple scales, and subsequently combined into separate Geographic Information Systems (GIS) coverages of mineralized veins and faults (Yager and Bove, this volume, pl. 1). The scale of data utilized ranged from 1:20,000-scale generalized geology for the western part of the Howardsville quadrangle and Silverton quadrangle (Luedke and Burbank, 1975a, b) to 1:250,000-scale geology compiled for intrusive rocks exposed in lower Cunningham Creek (Steven and others, 1974). Most data were compiled from 1:24,000-scale and 1:48,000-scale source maps (Lipman, 1976; Burbank and Luedke, 1964; Luedke and Burbank, 1987; Luedke, 1996). Due to (1) the numerous digital processing steps involved, (2) use of multiple software packages in digitizing source maps, (3) use of multiple map-scale source data, and (4) subsequent comparison and verification of digitized geologic features with paper maps, a final map scale of 1:48,000 was determined to be appropriate for the final geologic compilation (Yager and Bove, this volume, pl. 1).

Data Accuracy

Accuracy issues are important to consider when data of multiple scales are utilized in spatial analysis of geologic features. These issues are especially important when a GIS proximity analysis is done to determine how many structures or veins are within a specified distance from a linear feature or fault. A logical search distance was determined in this study based on the digital data sources utilized and on geologic field observations for the geologic features.

National Map Accuracy Standards (initially published by the National Bureau of the Budget in 1941 and revised in 1947) established that for map scales that are larger than 1:20,000, ninety percent of all features mapped must be within 1/50 of an inch of their actual locations on the map. A map that is published at the 1:48,000 scale has a map accuracy on the ground of 80 feet (about 24 m), whereas a map scale of 1:24,000 has an accuracy on the ground of 40 feet (about 12 m).

Other source data utilized include high-resolution U.S. Geological Survey digital orthophoto quadrangles (DOQ). The DOQs became available near the end of this study, after the geologic compilation was completed (Yager and Bove, this volume, pl. 1). The accuracy of these data is equivalent to 1:24,000 scale, that is, about 12 m. The area of the ground represented by each DOQ pixel is 1 m. Although these high-resolution images are very useful for interpreting structural information, a finer resolution data set is not necessarily directly applicable for comparison with geologic data that were compiled at a coarser scale.

The geologic structure data used in this study were obtained from the digital coverages used to create plate 1 (Yager and Bove, this volume, pl. 1). Separate digital GIS coverages of mapped faults and mineralized veins were combined to produce a single vector data file because, in many cases, mineralization in the study area occurred not only in veins, but also in faults where displacement and offset are evident. The combined vector coverage was then used to generate a raster data set with a 2-pixel width proximity zone around each line depicting mapped structure (fig. 3). A 20 m (2 pixels on each side of the mapped line) search distance is conservatively consistent with the 24 m accuracy of a 1:48,000-scale map product and reflects the approximate widths of structural zones observed in the field.

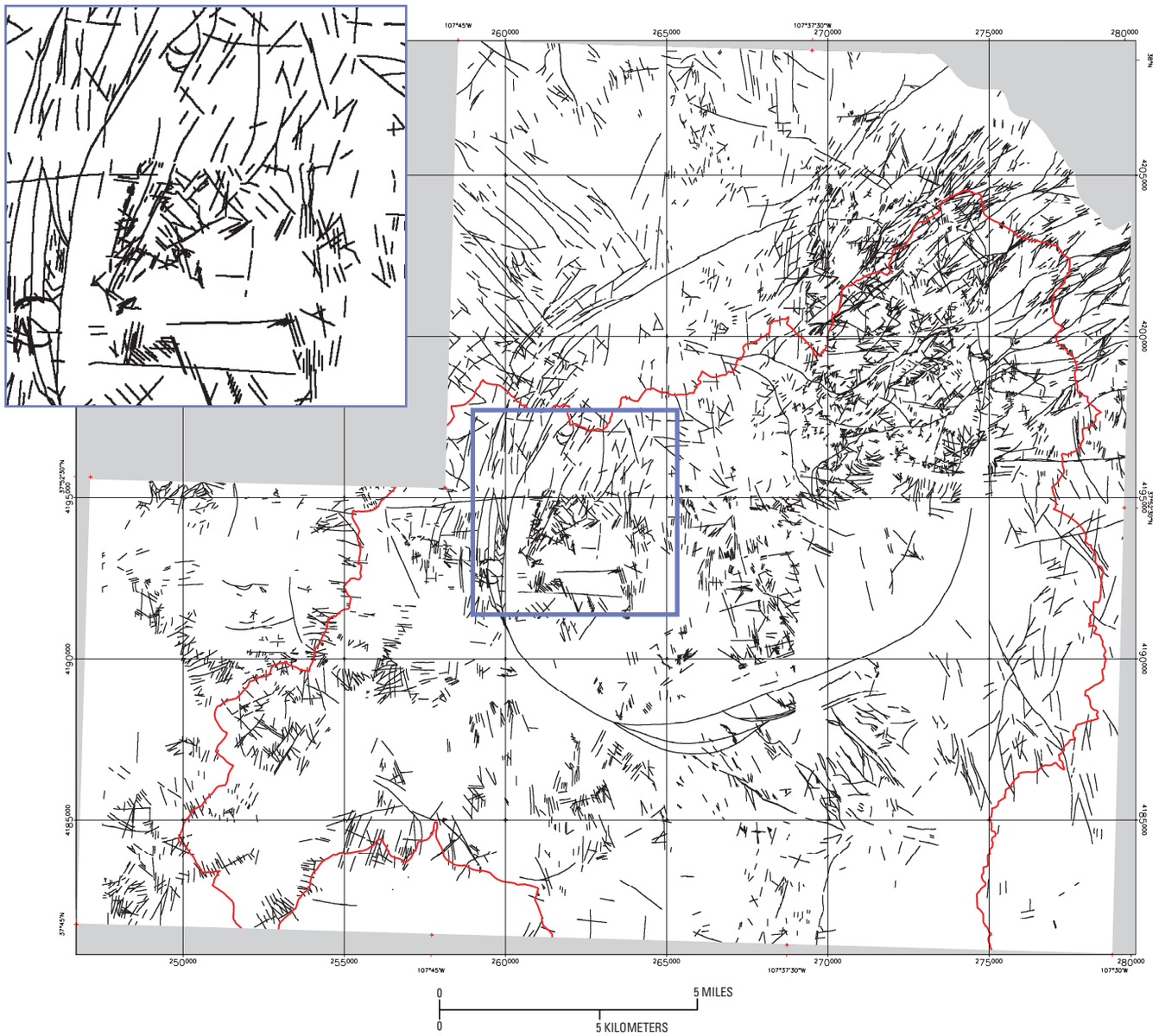

Figure 3. Mineralized and nonmineralized faults and veins (Yager and Bove, this volume, pl. 1). Unmapped areas shown in gray. Watershed study area boundary shown in red. Example inset of mapped structures with proximity zone is outlined in blue.

Remote Sensing Data

As part of the Animas River watershed study, two flightlines of AVIRIS (Airborne Visible Infrared Imaging Spectrometer) data were acquired in June 1996 by the Jet Propulsion Laboratory (JPL). The extents of coverage, processing of data, and mapping procedures are described by Dalton and others (this volume, Chapter E2). For the purposes of this investigation, the mapping results showing acid-generating and acid-neutralizing mineral assemblages were chosen to characterize geologic structures in terms of their AGP (acid-generating potential) (fig. 4) and ANP (acid-neutralizing potential) (fig. 5). Knowledge of the distribution of these mineral assemblages and their spatial association with structure is important to our understanding of the mineralogic character of possible ground-water pathways.

Alteration types in the study area, in order of weakest to most intense, include regional propylitic, weak sericite-pyrite, vein-related quartz-sericite-pyrite, quartz-sericite-pyrite, and acid-sulfate (Bove and others, this volume, Chapter E3). Most of the volcanic rocks in the watershed are propylitically altered, with pervasive secondary replacement minerals of chlorite, epidote, calcite, and locally sericite. The widespread propylitic alteration is significant because of the high acid-neutralizing potential (ANP) of calcite, and to a lesser extent, chlorite (Desborough and Yager, 2000).

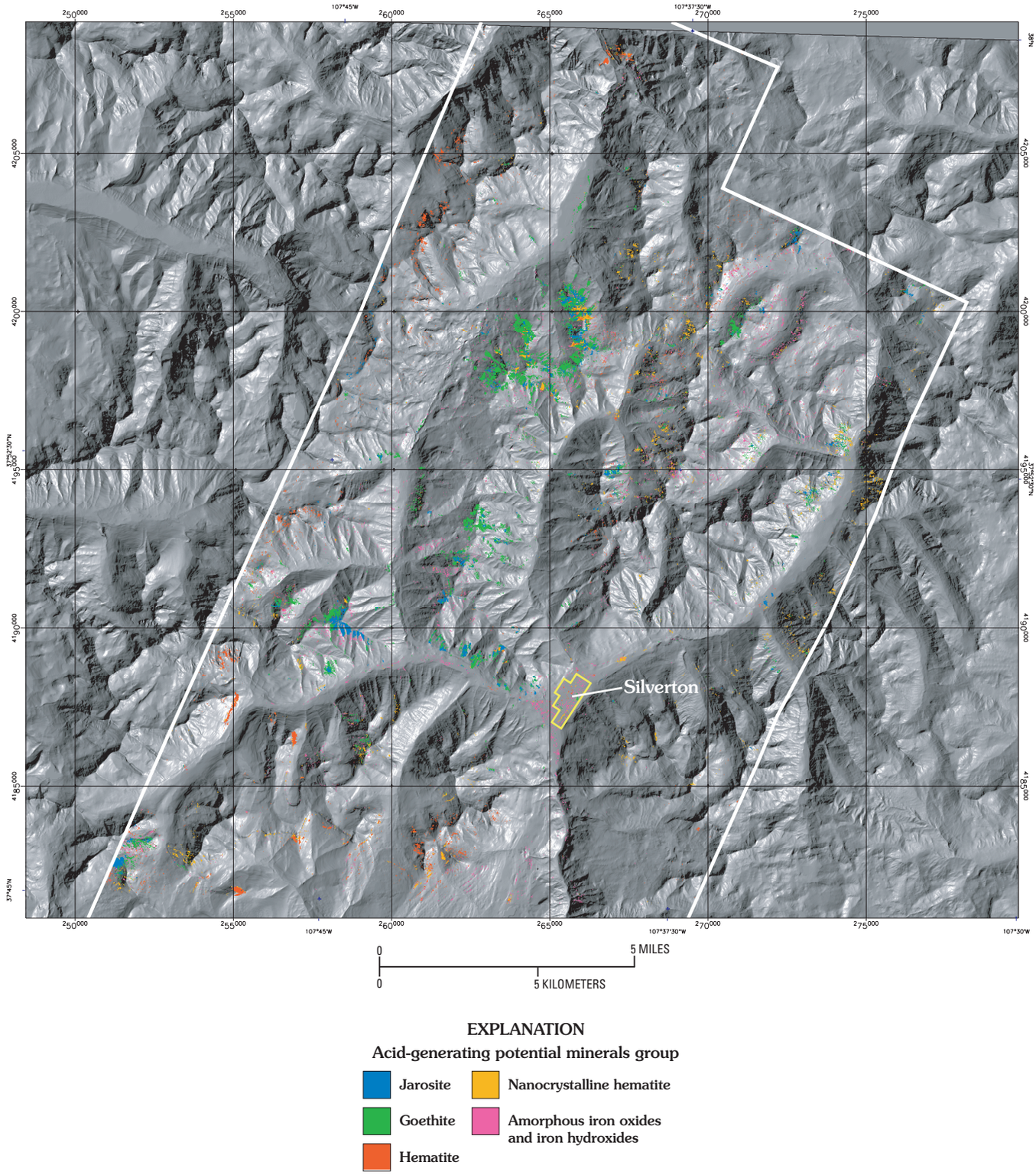

Figure 4. AVIRIS mineral map (white outline, extent of data) showing acid-generating potential (AGP) minerals. Base image is a shaded relief generated from the DEM (from Dalton and others, this volume, Chapter E2).

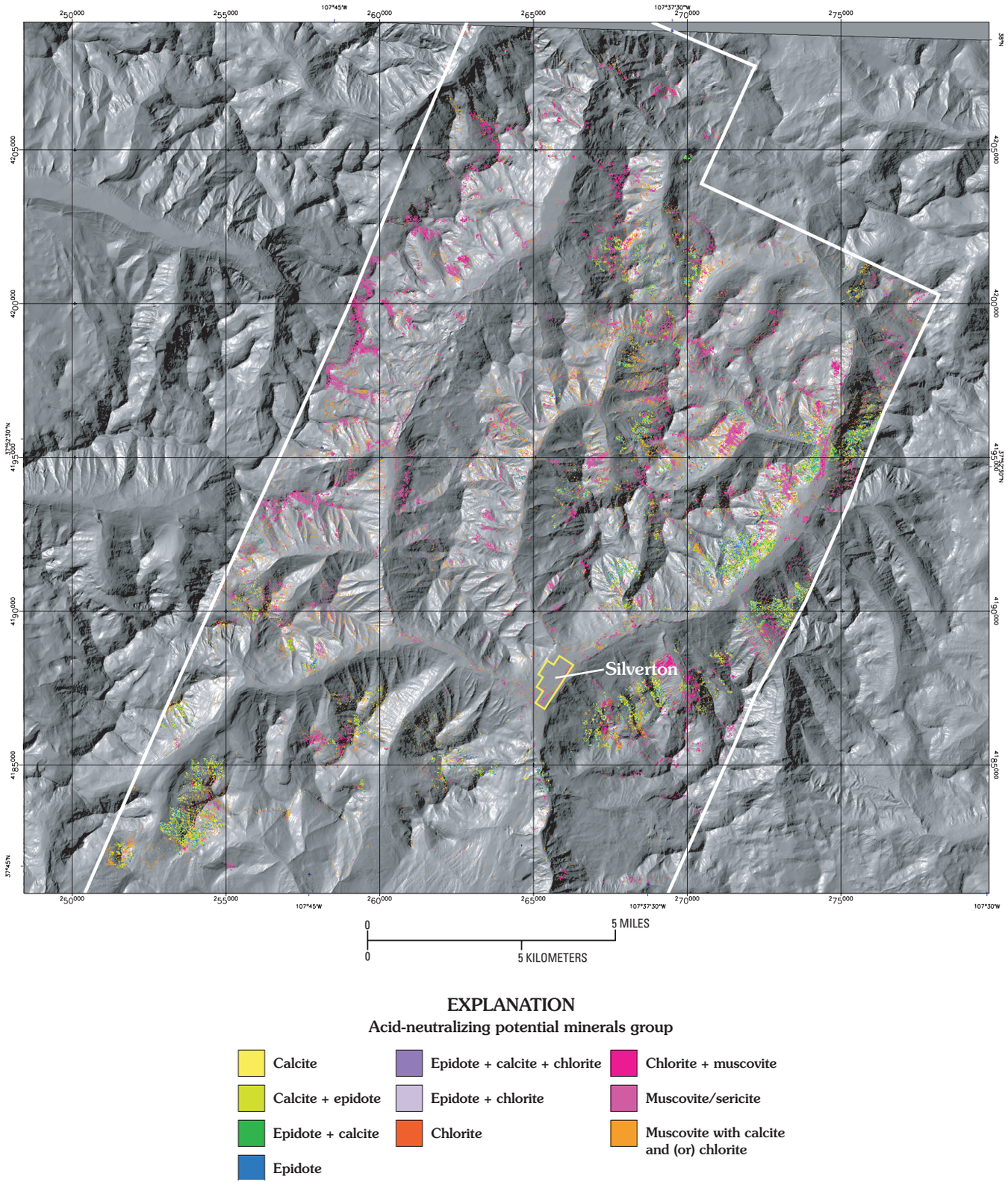

Figure 5. AVIRIS mineral map (white outline, extent of data), showing acid-neutralizing potential (ANP) minerals. Base image is a shaded relief generated from the DEM (from Dalton and others, this volume, Chapter E2).

The most significant acid-generating potential in the watershed is attributable to the weathering of pyrite. The AGP group includes jarosite, goethite, hematite, and amorphous iron oxides and hydroxides. Although these minerals themselves have generally low acid-generating potential (Desborough and Yager, 2000), they can indicate areas of greater potential for acid generation because of their association with pyrite in the weathering process. Pyrite itself is not included in the AGP group because, spectrally, it is difficult to map at AVIRIS resolution.

The ANP group of minerals spectrally detectable using AVIRIS data includes calcite, chlorite, epidote, and muscovite/sericite. The distribution of calcite, particularly in relation to faults and veins, is important because of its high ANP of acidic waters resulting from pyrite weathering and acidic runoff (Church and others, 2000). Chlorite also has some ANP though it is much less effective than calcite (Desborough and others, 1998). The mineral assemblage of calcite-chlorite-epidote occurs in areas of propylitic alteration and is indicative of areas of greater ANP. The combination muscovite/sericite is included in the ANP group because of its spectral relationship with and effect on the calcite-chlorite-epidote assemblage (Dalton and others, 2002).

Methods

Calculation of Planimetric Orientation of Structures and Geophysical Gradients

To evaluate similarities between planimetric orientations of mapped structures and structures at depth, generalized trends of mineralized faults and veins were compared to orientations of geophysical gradients. Gradients were calculated from the residual reduced-to-pole (RTP) magnetic data and the 4,310 Hz frequency electrical resistivity data following the method of Grauch (1988). Magnetic and resistivity gradients result from contrasts in magnetic and electrical properties of rocks, respectively, and map boundaries between rocks with dissimilar geologic characteristics. Geophysical gradient trends are defined as distinct linear and curvilinear elements that can be mapped from contours in the geophysical data. Faults and mineralized veins can be characterized by low electrical resistivities (high conductivity) if the structures contain clay, contain metallic minerals, or are filled with water containing high dissolved solids. Alternately, fractures that have been silicified or contain fresh water are commonly resistive. In general, dry, unfractured rock will have high resistivity values in contrast to its wet and fractured counterpart. If clays are present in fractured rock, and water is present, resistivity values can drop significantly (Olhoeft, 1985) in comparison to completely dry rocks.

The vector coverages of faults and mineralized veins (Yager and Bove, this volume, pl. 1) were simplified so that long curvilinear lines could be represented as straight-line segments and the geographic coordinates of the endpoints could be recorded. The geographic coordinates (recorded as Universal Transverse Mercator (UTM) coordinates) of the endpoints of each mapped vector were used to calculate the azimuth of each mapped structure. These data were used in a 2-D orientation analysis (Rockworks™, Rockware® Inc., 1999) to determine primary orientations of faults and mineralized veins from rose diagrams.

Predictive Modeling Methodology

A statistical approach using methodology developed by Lee and others (2001) for a statewide geoenvironmental assessment of Montana was applied to the geologic structure, topographic, geophysical, and mineralogical data layers in our study. The approach uses a ratio of probabilities to describe the statistical likelihood that a class within a particular evidential layer has a spatial association with a given prototype area. In this study, the prototype area is the area around and including the mapped faults and veins together with the 20 m proximity zone surrounding them. The probability ratios are expressed as weights of association, W. The expression for this weight is given by:

$$W = \frac{\text{Conditional Probability}}{\text{Prior Probability}}$$

In practice, the formula used to determine (W) is as follows:

$$W = \frac{\begin{array}{c}\text{(areas of overlap between an evidential}\\ \text{layer class and a prototype layer /area that}\\ \text{a test class occupies in the overall study area)}\end{array}}{\begin{array}{c}\text{(area that the prototype layer occupies}\\ \text{in the overall study area /}\\ \text{total area of the study)}\end{array}}$$

The probability ratio is expressed as the ratio of the probability of being in the prototype area given the condition of being in the test area (numerator) to the probability of being in the prototype area with no condition except being in the study area (denominator). In other words, the relative likelihood of finding the prototype (geologic structures) within each evidential (profile convexity, resistivity, magnetics, and mineralogy) class area is measured compared to the probability of finding the prototype within the study area (Lee and others, 2001). Weights fall within three categories that describe the spatial associations between evidential data layers and geologic structures.

A positive spatial association exists if W>1;

A negative spatial association exists if W<1; and

A random association is present if W=1.

For example, a probability ratio of 30 for a data layer class suggests that an observer is 30 times as likely to be within 20 m of a geologic structure if located within that class than if randomly (unconditionally) located within the study area. For this study, the topographic expression, magnetic properties, electromagnetic resistivity, and mineralogical characteristics (evidential layers) are evaluated for their spatial association with mapped geologic structures. The assumption is made when applying the probability ratio method that the training area (reference or prototype) accurately and adequately represents what the models are meant to predict.

The probability ratio method requires that the maps being compared be equal in their areal extent. If a data set lacks information over a particular region, the area analyzed is restricted to the region of overlap. All processing steps for the probability ratio method (Lee and others, 2001) were completed using GIS analysis tools in ERDAS® IMAGINE v. 8.5.

Data Preparation for Predictive Modeling

Topographic Data

The profile convexity topographic model was produced from a USGS digital elevation model (DEM) (10 m spatial resolution) using the commercially available image processing and analysis software package ENVI® v. 3.5 (Environment for Visualizing Images, Research Systems Inc.). The model measures the rate of change of the topographic aspect orthogonal to the *XY* plane. This parametric information is extracted by fitting a quadratic surface to the DEM data for a chosen cell size and taking the second derivative (Wood, 1996). For this study, it was determined that a five-by-five cell size sufficiently smoothed the DEM data without significant loss of topographic detail. The profile convexity image shows ridgelines as positive values (light values in image) and valleys and stream channels as negative values (dark values in image; fig. 6). The geologic structure data layer was used to mask the profile convexity data so that the two layers would have the same spatial extent, and therefore, could be compared on a pixel-by-pixel basis.

Magnetic Data Enhancement

Comprehensive discussion of the magnetic data acquisition can be found in Smith and others (this volume). Aeromagnetic surveying is based on mapping variations in the local magnetic field caused by changes in the surface and subsurface concentration of various magnetic minerals in rocks. Depth of investigation for magnetic data can vary from a few meters to hundreds of meters and is a function of anomaly wavelength. Shorter wavelength anomalies generally are produced by shallower magnetic sources, and longer wavelength anomalies represent the magnetic anomaly response of deeper buried features.

A number of data enhancement techniques are applied to the magnetic data to transform anomalies into a form that can be directly compared with variations in rock mineralogical properties. Enhancements were used that (1) reduce the magnetic field to the magnetic pole to position anomalies approximately over their causative sources; (2) increase the resolution of small-scale anomalies related to near-surface magnetic sources; and (3) enhance anomalies related to deep-seated crustal boundaries.

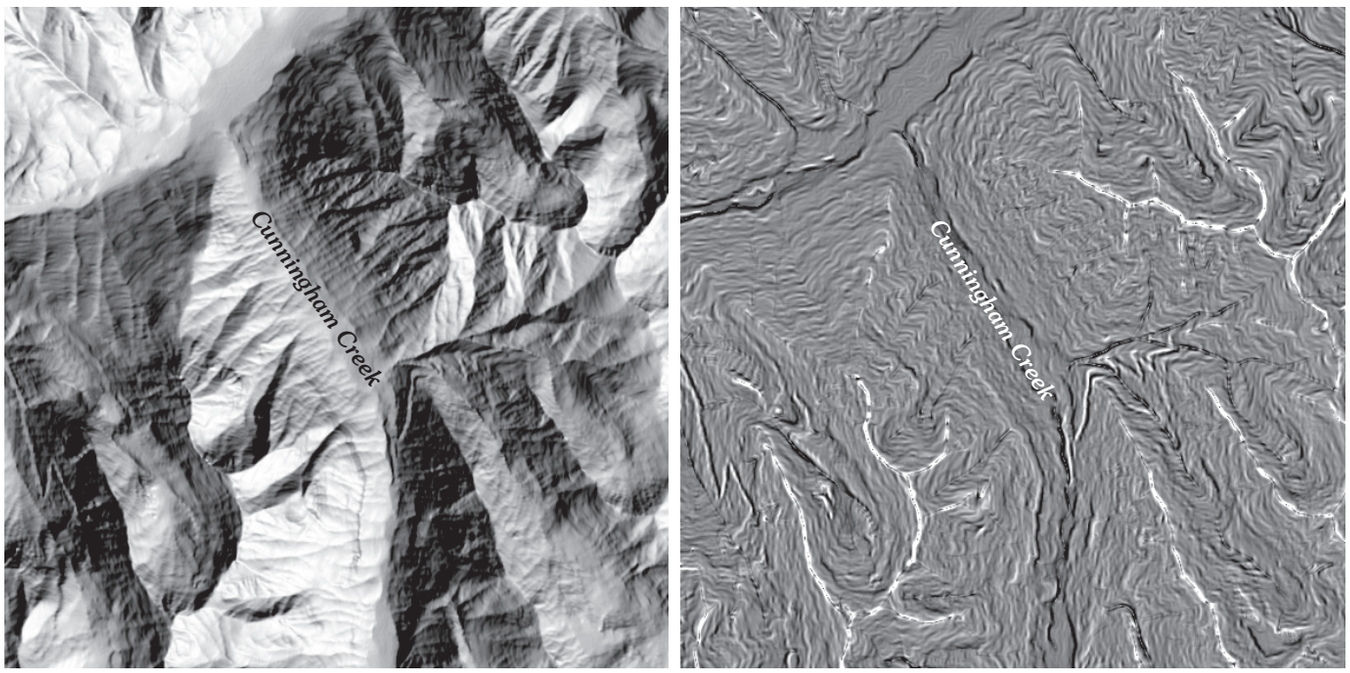

Figure 6. Example of shaded relief Digital Elevation Model (DEM) (left), and derived profile convexity model of corresponding area (right).

The study area is located at a geomagnetic latitude where magnetic anomalies are shifted slightly to the southwest from their sources and are represented by an anomaly pair determined, in part, by the inclination of the present-day Earth's field. To correct anomalies for this offset in symmetry and position, a filter called reduction-to-pole (RTP) was applied to the magnetic data for the watershed using U.S. Geological Survey potential fields programs (Phillips, 1997). Application of the RTP filter correctly positions magnetic anomalies over their sources. This assumes that the rock's total magnetization (sum of induced magnetization and remanent magnetization) is effectively collinear (coaxial) with the Earth's present field (Telford and others, 1976).

Although some rock units within the Silverton caldera (fig. 1) exhibit remanent magnetization (Gettings and others, 1994; Grauch and Hudson, 1987), the magnetization intensities and directions are low and within a range considered collinear with the present-day magnetic field (Bath, 1968). Consequently, we can consider the remanent magnetization negligible for purposes of this study and assume that for the majority of RTP magnetic anomalies, their shape and positions are accurately estimated (fig. 7).

To aid interpretation of anomalies related to near-surface geologic units, "match" filtering was applied to the RTP data. Match filters facilitate approximations of magnetic fields produced by sources at different depths based on ranges of wavelengths. The filtering was applied using a method developed by Syberg (1972), and was implemented with U.S. Geological Survey computer programs by Phillips (1997). Application of this method yielded a short-wavelength anomaly field that approximates the magnetic response from a shallow magnetic source layer located approximately in the upper 200 m of the topographic surface. The magnetic response from the shallowest depth layer, defined as the "high-pass" magnetic anomaly, relates to near-surface geologic units and processes important to this study (fig. 8). The depth range of the shallowest magnetic-source layer corresponds most closely to the apparent-resistivity-data depths of investigation and to acid-generating and acid-neutralizing interactions.

A second product of match filtering is a long-wavelength component of the RTP magnetic field (fig. 9). Anomalies in this map represent the magnetic response of rocks at depths exceeding approximately 1,300 m. This estimate is given as part of the matched filtering process and is based on theory discussed in Syberg (1972). The magnetic response from the deepest sources, defined as the "low-pass" magnetic anomalies, is likely associated with features such as the structural boundary of a caldera.

In broadest terms, magnetic anomaly maps depict anomalies and the gradients that separate them. The characteristics of a magnetic anomaly are its amplitude and wavelength, which are functions of the amount of magnetic minerals (commonly titanomagnetites) present in the rock and the depth to the magnetic source. The gradients that surround magnetic anomalies map lateral discontinuities among rocks with different magnetic properties. These gradients can be related to faults and structures that juxtapose rocks with different magnetizations.

To enhance the locations of magnetic boundaries and to evaluate directional trends within the magnetic anomaly maps as they relate to geologic structural trends, a three-step procedure was applied to both the high-pass RTP (fig. 8) and low-pass RTP (fig. 9) maps. First, the magnetic potential was calculated, originally called pseudogravity by Baronov (1957). The magnetic potential transformation reduces the side lobe gradients in RTP maps caused by magnetic sources with limited thickness (Blakely, 1995). The horizontal gradient magnitude (HGM) of the magnetic potential was then calculated following the method of Cordell and Grauch (1985). The HGM of the high-pass and low-pass magnetic potential field is shown in figures 10 and 11, respectively.

The HGM method objectively locates the steepest parts of gradients present in the magnetic potential data. In figures 10 and 11 magnetization boundaries are portrayed as elongate ridges. The ridge crests locate boundaries where rocks with significantly different magnetizations are juxtaposed. In general, this technique works on the premise that an anomaly slope (either positive or negative) will be steepest at a point directly over a vertical or near-vertical geologic contact. The positions of the ridge crests can be offset somewhat if the contact is gradational or not steeply dipping, if the magnetic source was under-sampled, or if there are a number of magnetic sources superimposed (Grauch and Cordell, 1987). Examples of the magnetic data transforms just described are shown in figure 12.

Due to the dissimilar areal coverage (fig. 2) of the geologic structure and airborne magnetic data sets, a two-step masking process was used to produce raster layers of equal spatial extent. First, the geologic structure layer of faults and veins was used to mask the magnetic data layer. The resulting layer of magnetic data was then used to mask the original layer of faults and veins.

Electrical Resistivity Data

The airborne electromagnetic system maps the lateral and vertical variations in electrical resistivity (or the reciprocal, conductivity) of rocks, structures, and soils. The depth of investigation for the EM measurements varies inversely as a square root of frequency and ground resistivity (Telford and others, 1976). The electromagnetic (EM) field was measured with three frequencies (984, 4,310, and 36,000 Hz) using horizontal coplanar transmitting and receiving coils. Discussion of the electromagnetic data acquisition and processing can be found in Smith and others (this volume).

For this study, the mid-frequency 4,310 Hz data were used to investigate the resistivity characteristics of structures to an approximate depth of 50 m (fig. 13). The structures in this depth range are likely those that would be associated with shallow to mid-depth structurally controlled ground-water flow. The same two-step masking procedure used for the magnetic data set was also applied to the resistivity data.

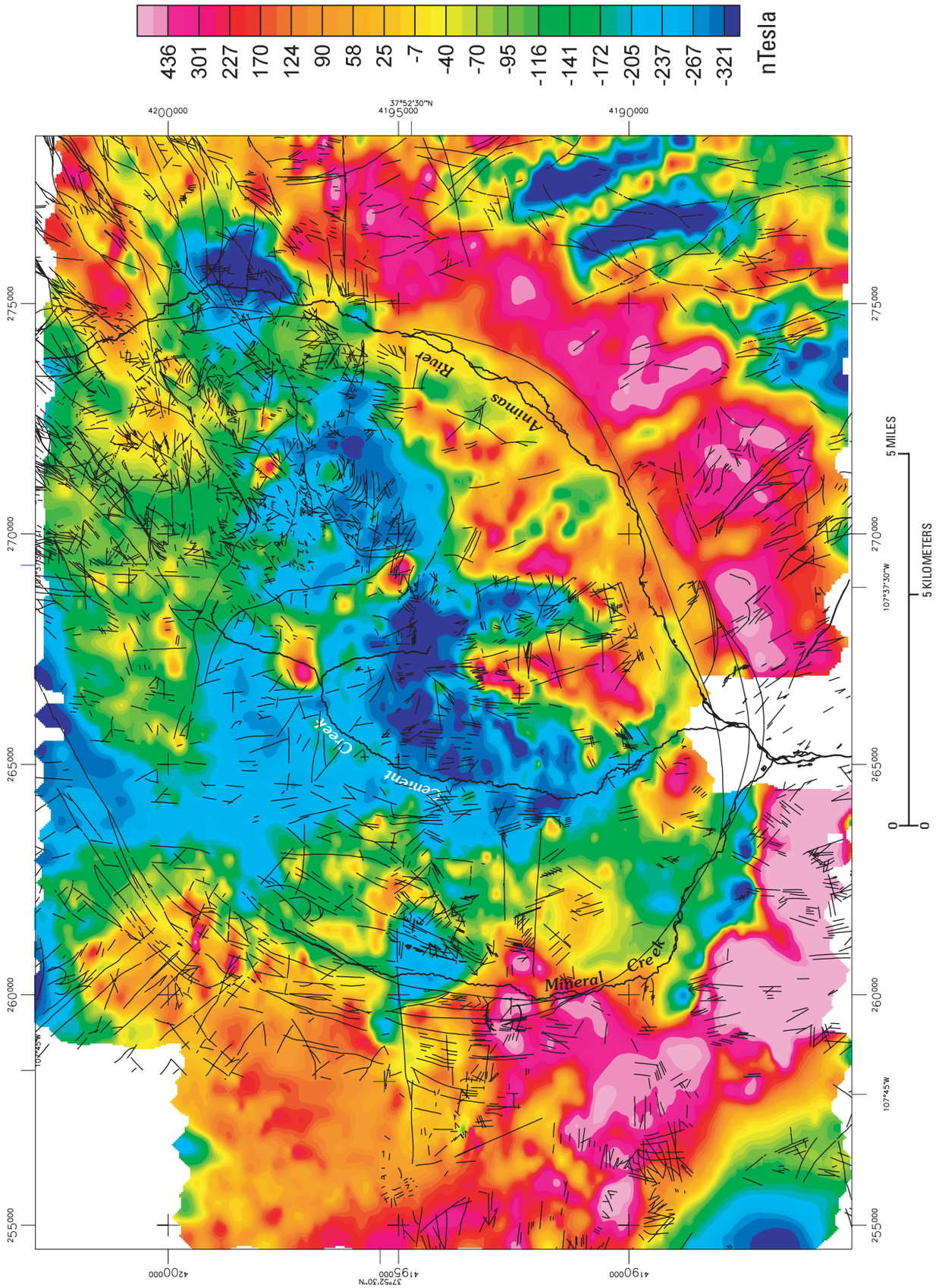

Figure 7. Reduced-to-pole magnetic anomaly map. Data from this map were filtered to enhance magnetic features located in the shallow and deep crust (figs. 8 and 9, respectively). Map of mineralized and nonmineralized faults and veins (Yager and Bove, this volume, pl. 1) is overlaid on the magnetic data map.

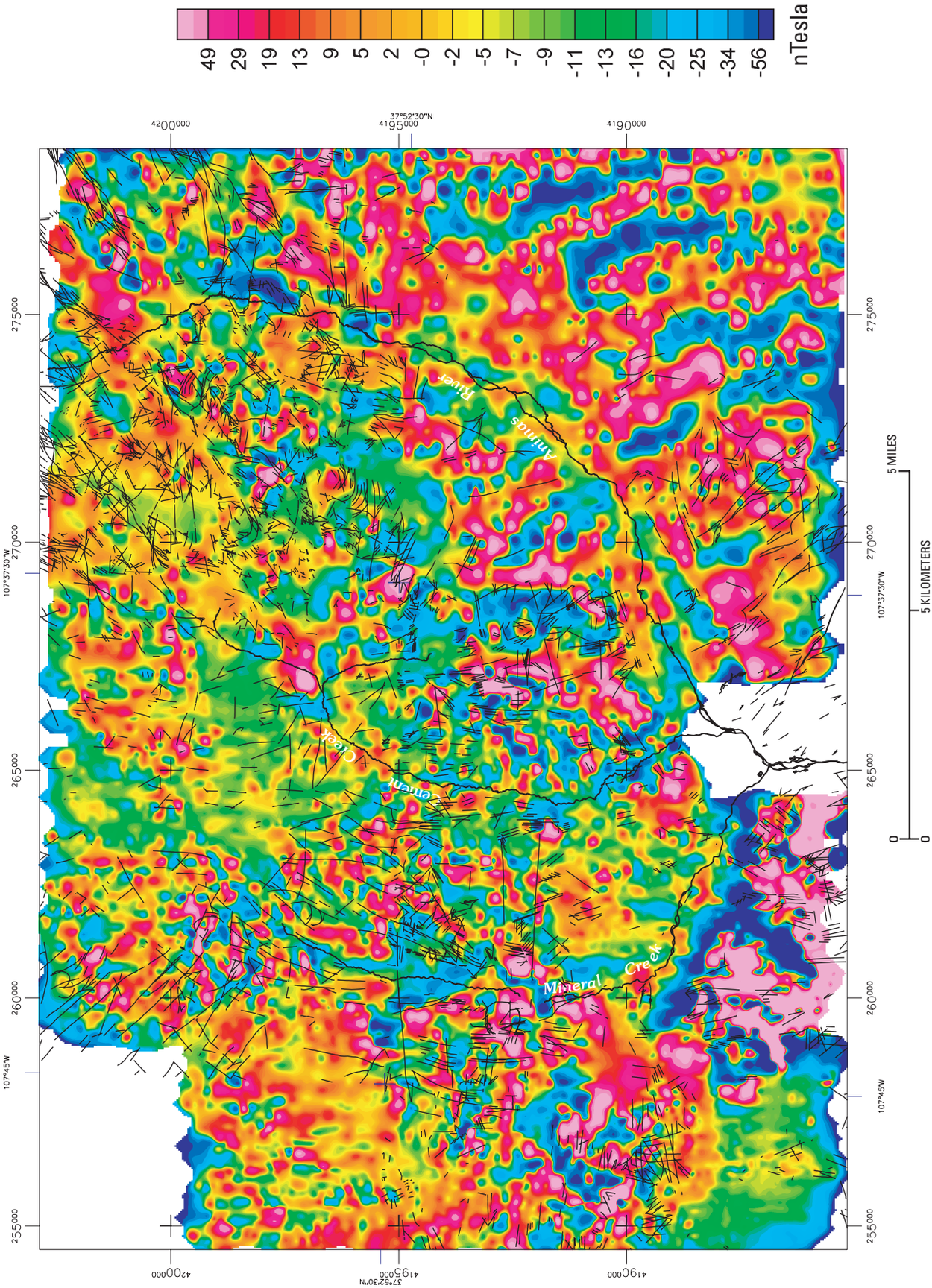

Figure 8. "High-pass" filtered magnetic anomalies calculated from RTP magnetic data (fig. 7). Map shows magnetic anomalies in the shallow crust as related to mineralized veins (black lines).

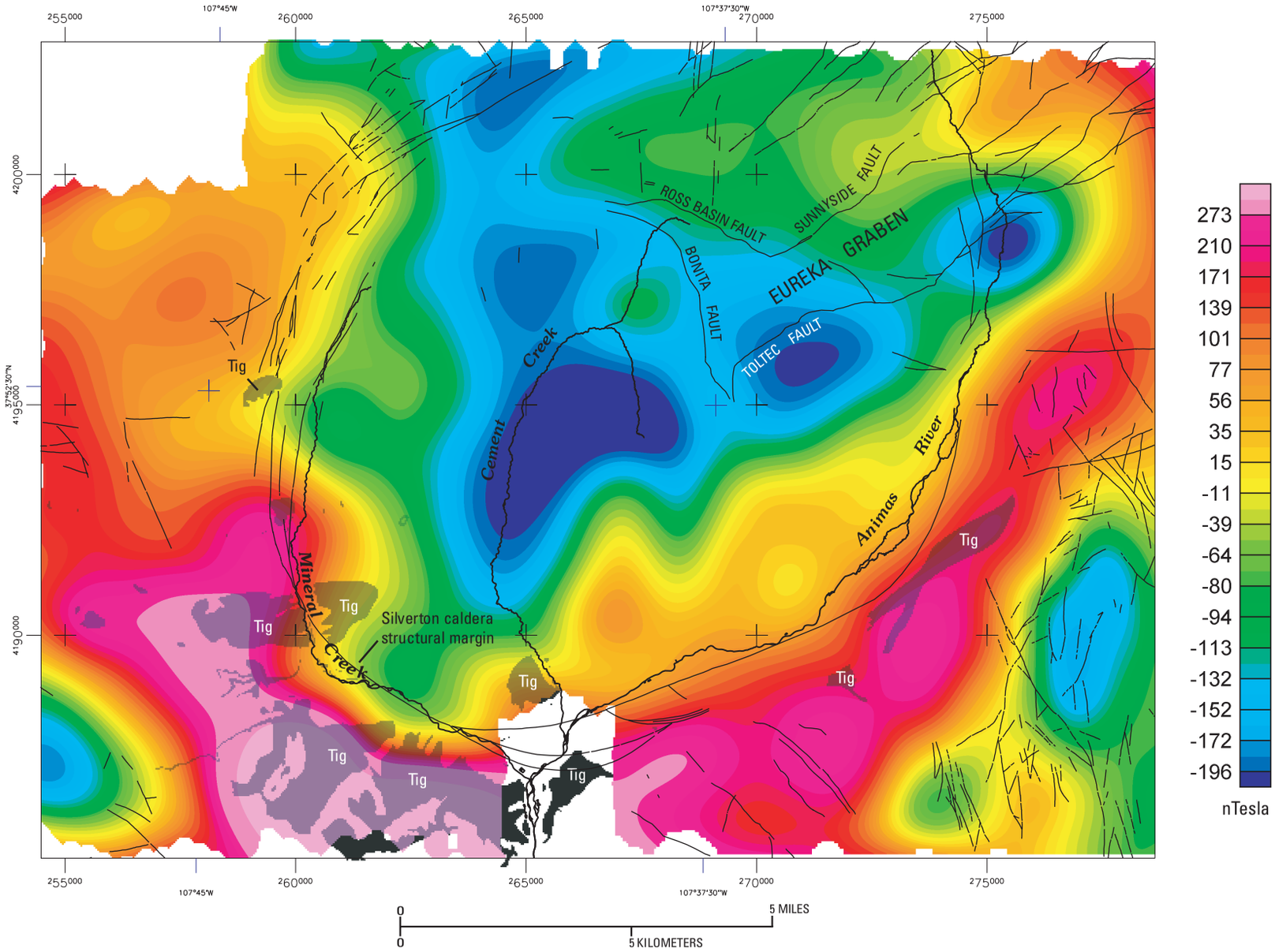

Figure 9. "Low-pass" filtered magnetic anomalies. The filter enhances anomalies associated with magnetic properties of deep crustal features. The Sultan Mountain stock granitic intrusives (Tig) are shown in black and gray, and major structural features are also shown.

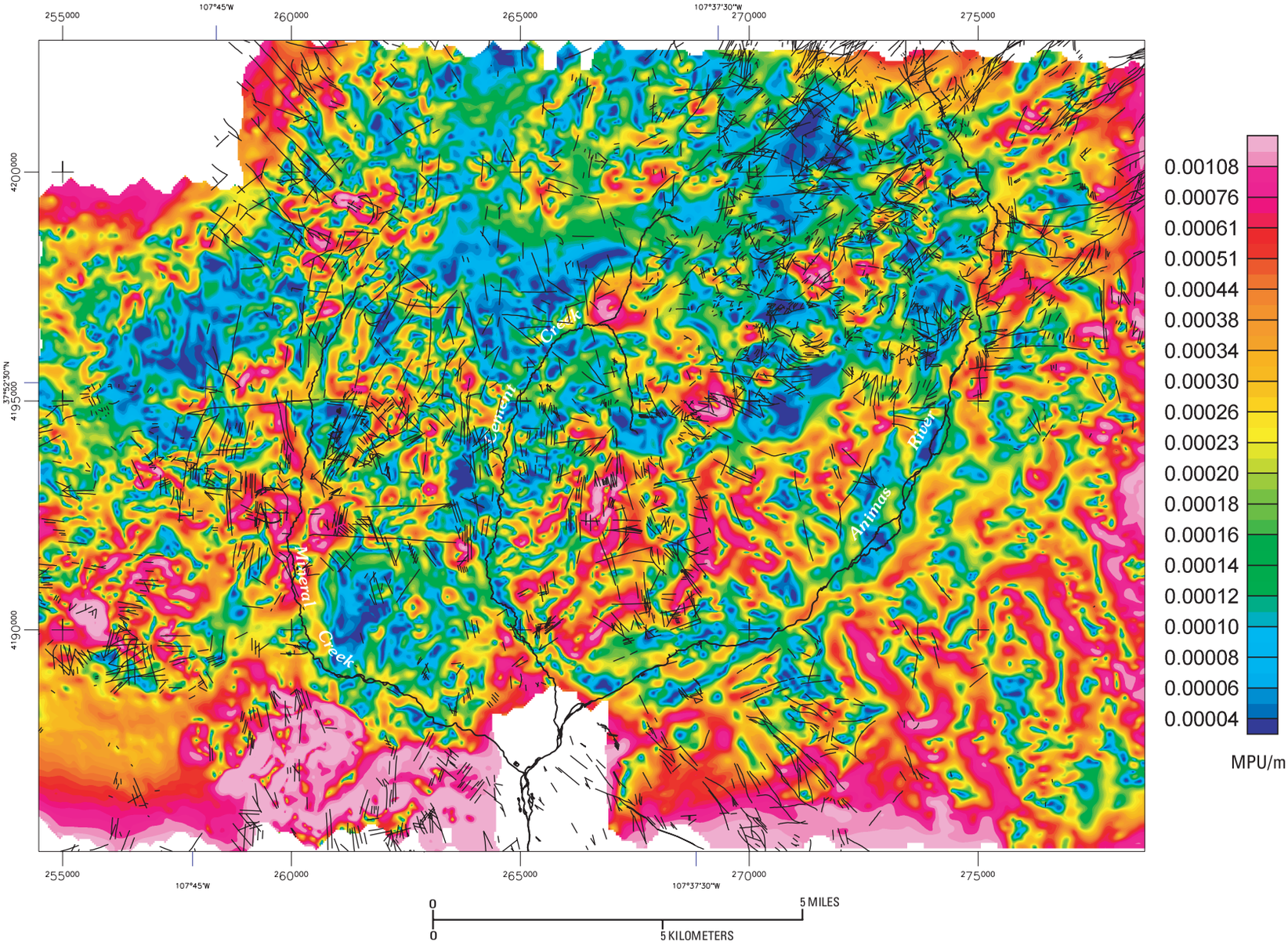

Figure 10. "High-pass" horizontal magnetic gradient (HMG) anomalies calculated from RTP magnetic data (fig. 7). Map shows magnetic gradients in the shallow crust as related to mineralized veins (black lines). MPU, magnetic potential units.

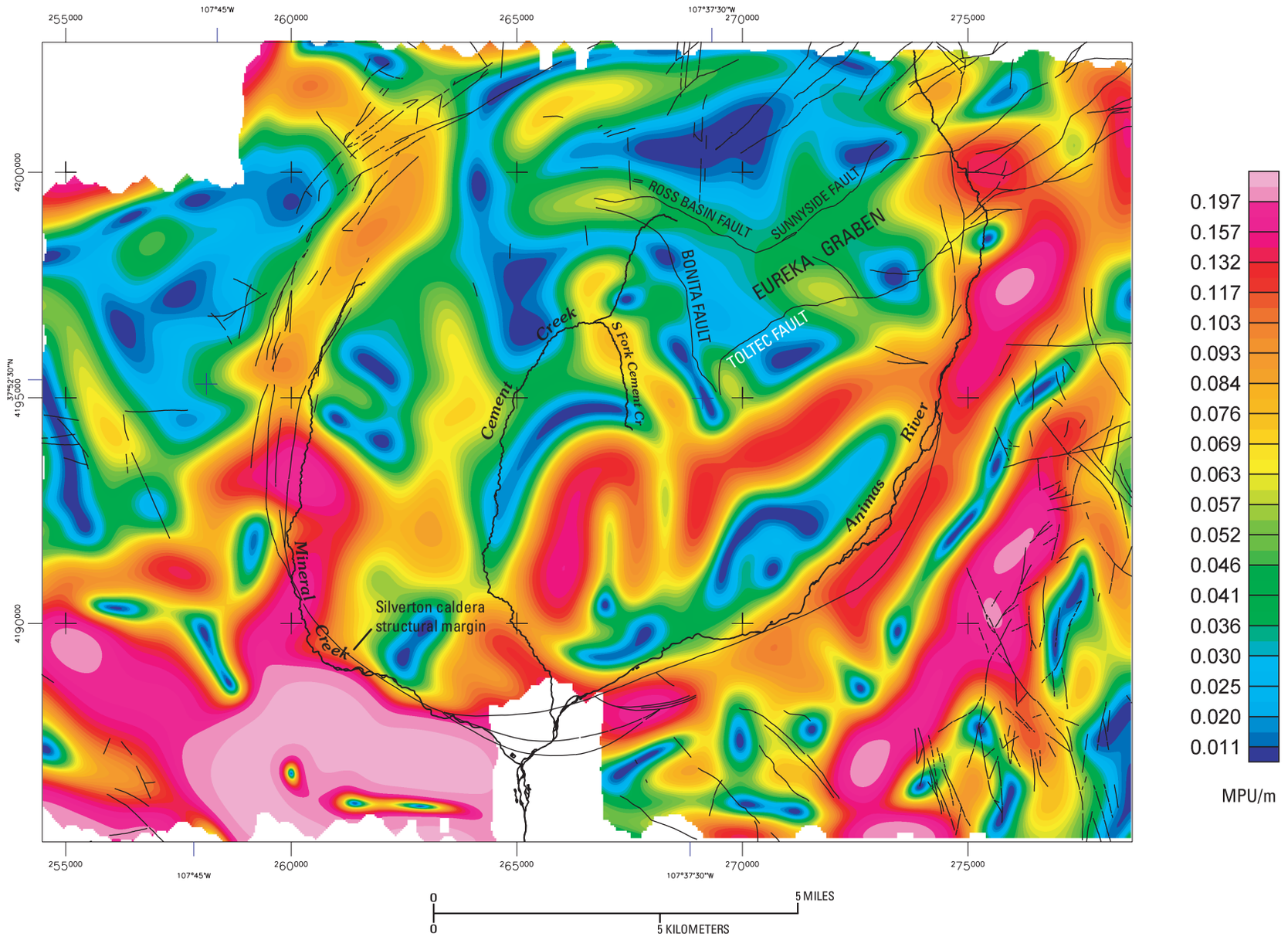

Figure 11. "Low-pass" horizontal magnetic gradient (HGM) anomalies calculated from RTP magnetic data (fig. 7). Map shows magnetic gradients in the deep crust. Major faults are shown as black lines. MPU, magnetic potential units.

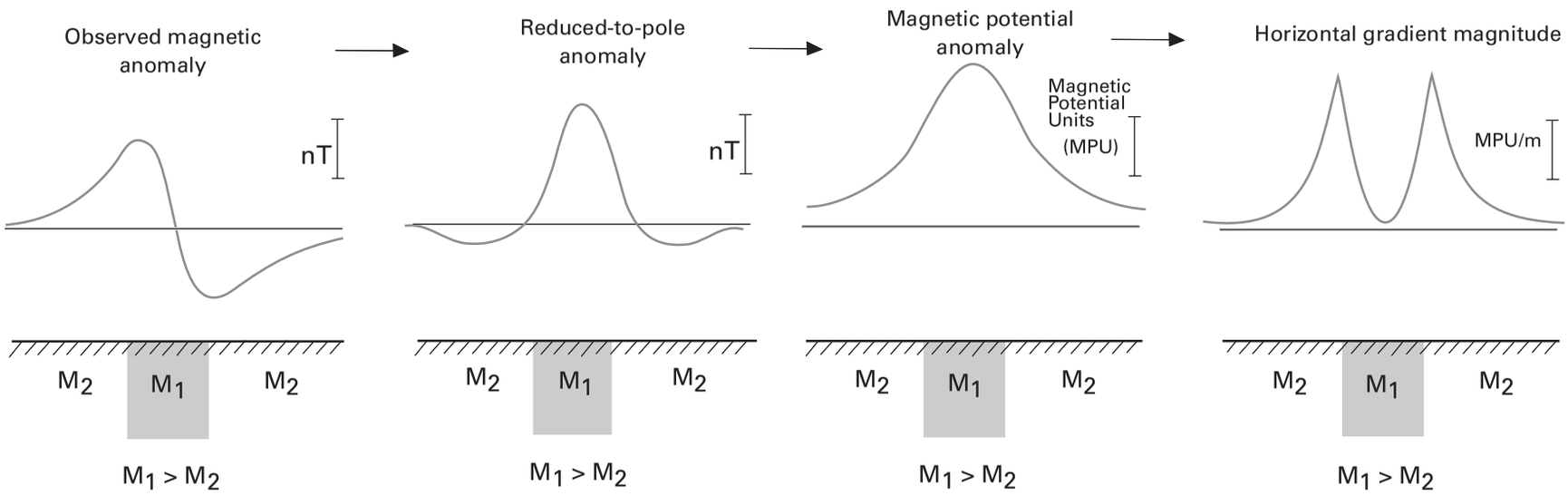

Figure 12. Profile illustration of various transformations applied to the Silverton magnetic data. A theoretical geologic cross section is shown below geophysical profiles to illustrate the geophysical signature of the transformations. The geologic cross section depicts a rock unit with higher magnetization (M1) juxtaposed next to a unit with lower magnetization (M2).

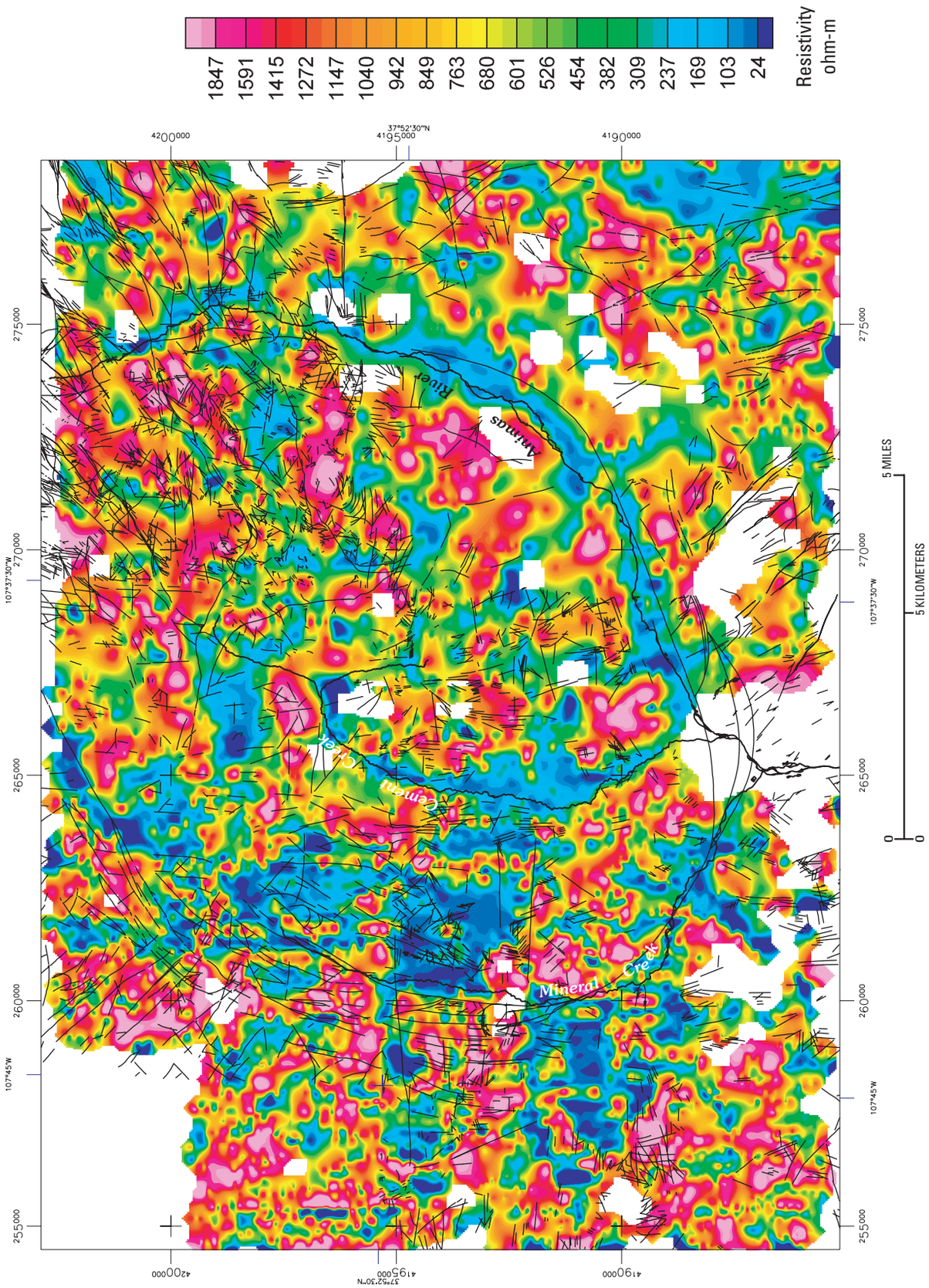

Figure 13. Map of 4,310-Hz apparent resistivity data showing lateral variations in electrical resistivity of rocks from surface elevations to approximate depths of 50 m. Data from this map are used to define resistivity characteristics of geologic structures.

Remote Sensing Data

The AVIRIS flightlines extend well to the southwest beyond the watershed boundary (fig. 2). Therefore, the AGP and ANP mineral maps were masked to correspond with the extents of the mapped faults and veins.

In addition to the data layers of acid-generating and acid-neutralizing minerals previously described, a map of vegetation and snow cover was also produced from the AVIRIS data set (Dalton and others, this volume). For the purposes of this study, this map represents areas where the spectral signals of minerals are obscured, or in this case, represent areas of "no data." As with the electrical resistivity data where the sensor was out of range with the ground, it was necessary to omit these areas from the probability ratio calculations. In order to mask the coverage of mapped faults and veins, we converted the vegetation and snow cover data from a red-green-blue (RGB) image to a binary data file (fig. 14). The mapped faults and veins data layer was then masked using the extents of the AVIRIS data. Finally, the resulting structural data layer was masked using the binary layer of vegetation and snow cover.

Results and Analysis

Planimetric Orientation of Geologic Structures and Geophysical Gradients

The planimetric orientations (orientation in the *XY* plane) of geophysical gradients were compared to trend orientations of mineralized faults and veins to determine if mapped surface geologic structures are parallel to magnetic and resistivity trends caused by subsurface features. The orientations are presented as rose diagrams that provide a straightforward means of comparison among the different data sets (fig. 15). Gradients of the residual reduced-to-pole field reflect changes in magnetic properties of rocks at the surface to depths of tens of kilometers, whereas the 4,310 Hz apparent resistivity data reflect gradients caused by lateral resistivity changes in rocks at the surface to depths of approximately 30 m.

Major northeast (approximately 45°), north (approximately 0°), and northwest (approximately 270°) structural trends are known to occur in the region of the Silverton caldera. Structural activity, throughout much of the geologic history of the region, has occurred along these trend lines (Burbank and Luedke, 1969). A prominent north-south (0°–10°) trend is observed in the mapped structure, which is parallel to the north-south trend observed in the magnetic and apparent resistivity gradients. This trend may be somewhat enhanced in the airborne geophysical data due to the north-south flightline direction. The resistivity data are more sensitive to this effect as evidenced by the north-south trends that occur along a few flightlines.

A northeast trend is prominent in the orientation of faults and is evident to a lesser degree in the orientation of mineralized veins (fig. 15*B*, *A*, respectively). This trend of faults is likely the expression of the structures of the Eureka graben such as the Toltec and Sunnyside faults (see Yager and Bove, this volume, pl. 1). A northeast trend is also indicated in the rose diagram of apparent resistivity (fig. 15*D*), with a minor northeast trend shown in the magnetic gradients (fig. 15*C*). The rose diagram of the apparent resistivity gradient (fig. 15*D*) shows a strong easterly trend, correlating with east-west-trending silicic structures (Burbank and Luedke, 1969) that are probably electrically resistive.

Weights Charts and Predictive Models

Modeling results are presented in two ways. The first is a chart showing probability weight values on the vertical axis versus evidential layer classes on the horizontal axis. Weights greater than 1 show where a range of data best characterizes the structures. Weights with values less than 1 indicate classes least likely to be associated with structures. Weights of zero value indicate classes in the evidential layers that had no overlap with geologic structures. Evidential layer classes with weights near 1 indicate that random spatial associations with geologic structures exist, and those layer classes are therefore not predictive of the presence or absence of veins or faults.

The second type of result of the modeling approach presented here is a predictive map. In the cases where a physical property characterized a prototype area, a predictive map was generated by redefining classes within the evidential layer in terms of their corresponding weights. Only classes with weights greater than 1 are shown. A weight greater than 1 indicates that a particular topographic, geophysical, or mineralogical class exhibits a positive association to the prototype area. Colors are used in the predictive maps to show areas with ranked potential for the target characteristics from least (blue) to best (red).

Profile Convexity Model

The first predictive model compares the map of mineralized and nonmineralized faults and veins (fig. 3) with the raster image of topographic profile convexity (fig. 6). The chart of weights of profile convexity (fig. 16) shows that structures are most likely to occur along sharp ridges or in proximity to stream channels and incised valleys. Structures are least likely to occur where the convexity is near zero, or, where the terrain is flat. In fact, where the convexity is near zero the weight is less than 1, indicating a negative association of structures to low topographic gradients. This suggests that mapped mineralized faults and veins in the study area are most likely to occur as either erosionally resistive, and likely silicified structures, or as eroded, and possibly altered structures.

The predictive model map (fig. 17) shows where unmapped structures are most likely to occur based upon their topographic signature. Highest probabilities are shown in red and lowest probabilities are shown in blue. Several examples show where the model predicts that stream channels or ridges

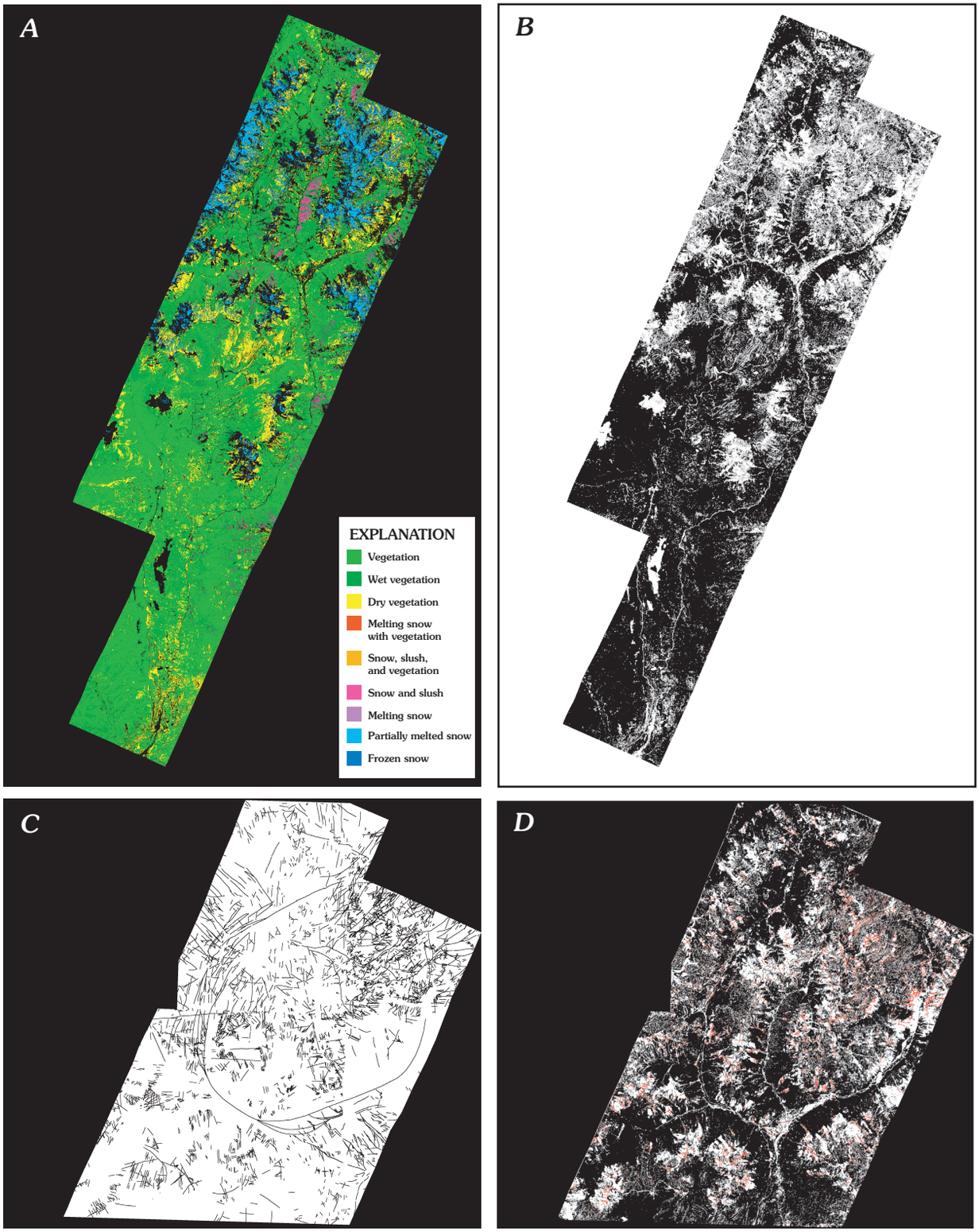

Figure 14. Data layers used to produce masked coverage of faults and veins from AVIRIS vegetation and snow cover mapping. *A*, The original map (from Dalton and others, this volume, Chapter E2). *B*, Binary mask produced from the vegetation map (black indicates areas of no mineralogical data). *C*, Mapped faults and veins masked using the AVIRIS data extents. *D*, The final masked coverage of mapped structure (red, structures; black, covered areas).

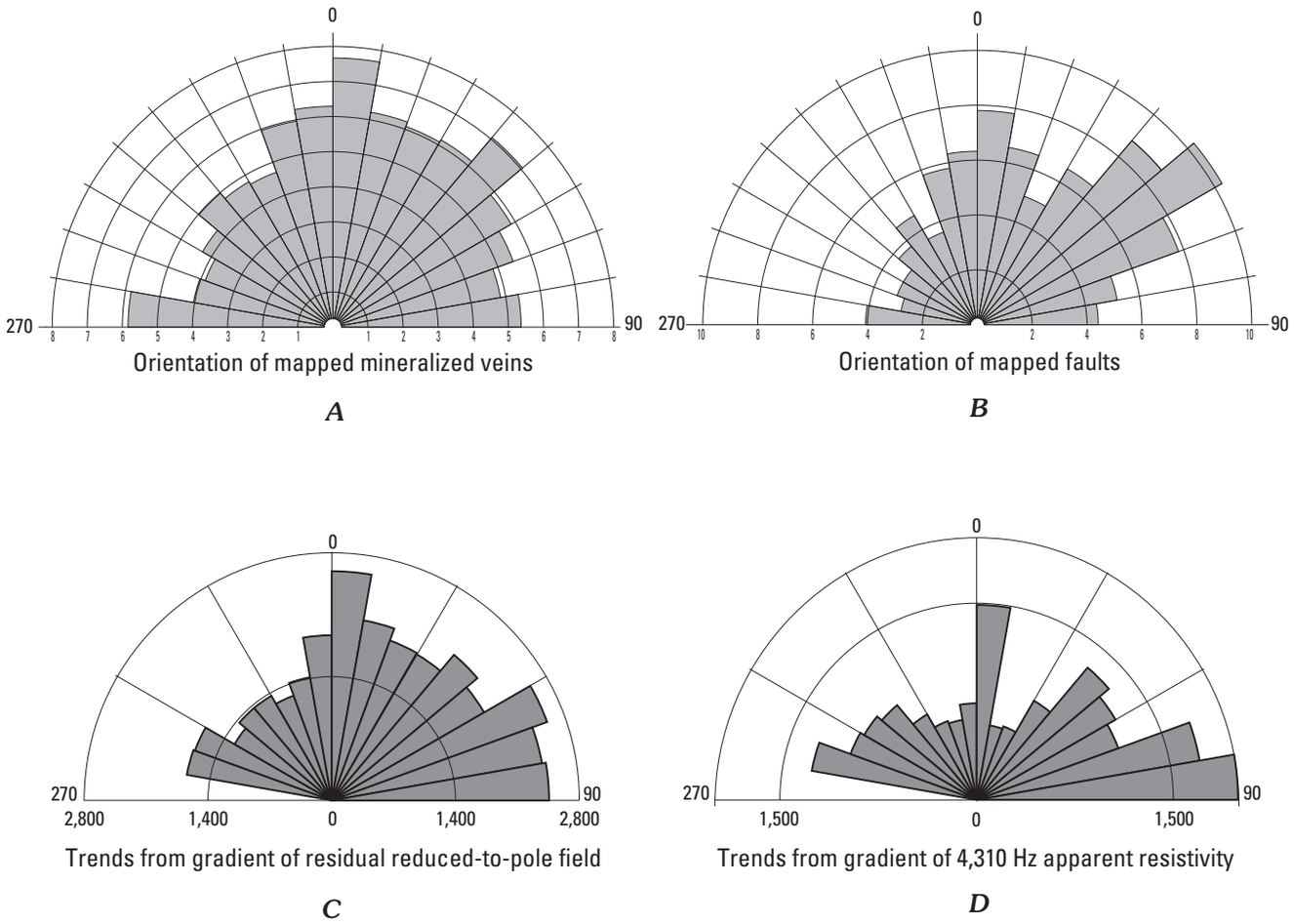

Figure 15. Planimetric orientation of mapped geologic structure (*A, B*), and geophysical gradient trends from airborne geophysical survey (*C, D*). Rose diagrams of mapped structures were calculated as class percentages; rose diagrams of geophysical gradients were calculated as number per class.

are most likely related to structures. Locality A (fig. 17), upstream of Chattanooga on upper Mineral Creek, has a high probability of association with structure and is mapped as a significant fault on the geologic map (Yager and Bove, 2002; Yager and Bove, this volume, pl. 1). High probabilities are also shown at B, near the confluence of Mineral Creek and South Fork Mineral Creek, and C, below Arrastra Creek; these are interpreted as structures associated with the structural margin of the Silverton caldera. Examples D, near the lower part of Cement Creek, and E, upstream of Animas Forks on the upper part of the Animas River, illustrate areas where faults have not been mapped, but these areas are predicted to be structurally controlled linear stream channels. Example F, near Storm Peak, is an area where numerous mineralized veins have been mapped (Yager and Bove, 2002; Yager and Bove, this volume, pl. 1). The profile convexity model suggests that these structures form erosionally resistive ridges and are therefore likely to be silicic in composition. The weights chart (fig. 16) shows that structures with similar positive convexity are more likely to occur in the study area based on their topographic characteristics.

Resistivity Model

Data from the 4,310 Hz resistivity grid were compared to mapped geologic structures to evaluate whether the structures have a characteristic electrical amplitude. Results show a strong association of moderately high resistivity with structure (fig. 18). The predictive map calculated from the statistical model (fig. 19) shows areas of higher weights that coincide with groups of structures. Whole rock chemical analysis of various members of Tertiary volcanic rock units show high weight percentages of silica (Luedke and Burbank, 2000), a correlation that is consistent with the high electrical resistivities that occur over parts of these units. Silica-rich rocks typically exhibit high electrical resistivities (Telford and others, 1976). The areas with high weights are interpreted to predict areas where silica-rich vein and volcanic mineralogy is predominant. In contrast, rocks that have undergone extensive hydrothermal alteration likely develop more clays and will map as low resistivity regions (structures within the gray areas in fig. 19). Areas where mapped structure does not coincide with high weights in the predictive model may

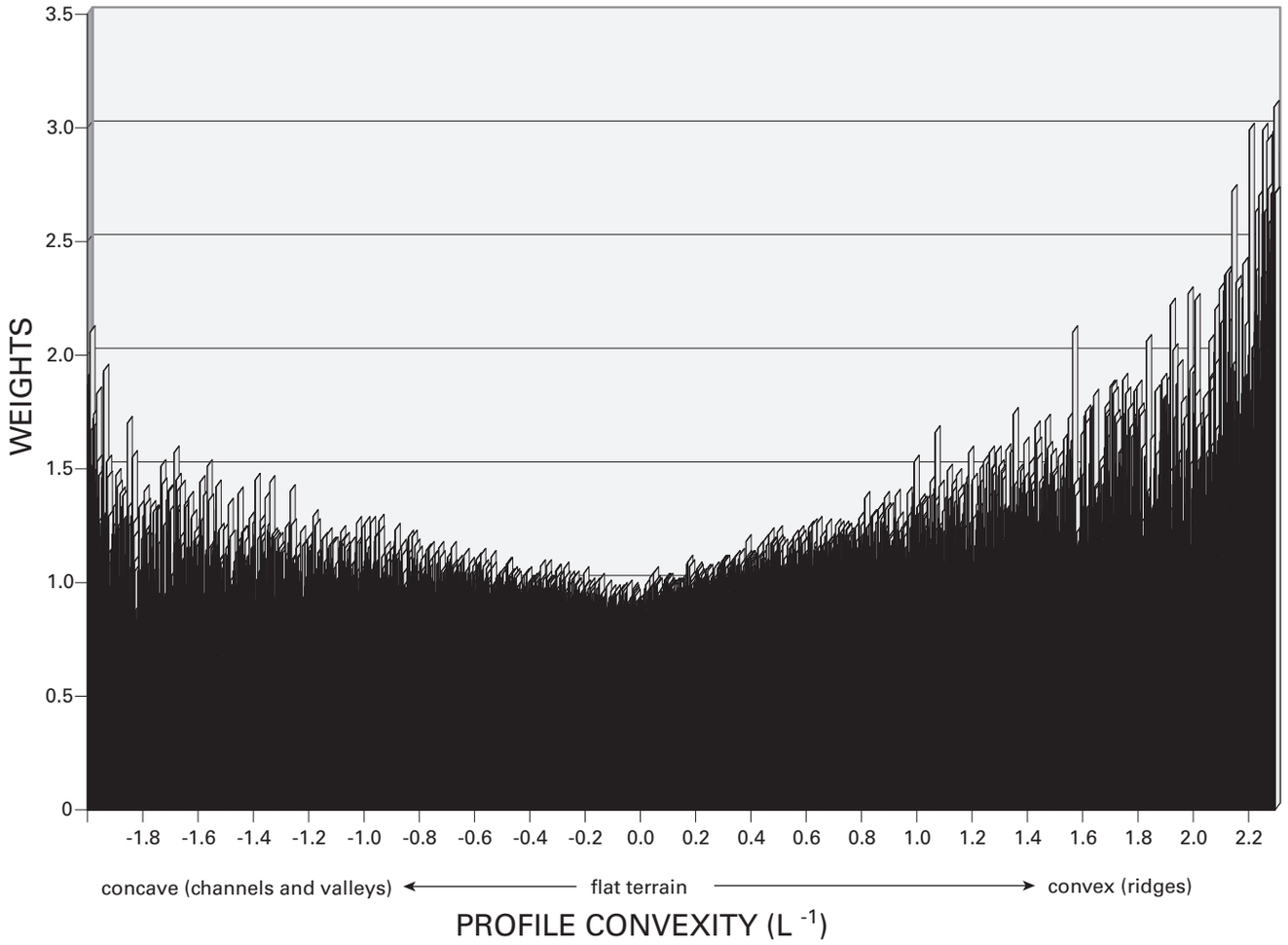

Figure 16. Calculated weights of the relationship of structures to topography. Negative values indicate increasing concavity or channels; positive values indicate increasing convexity or ridgelines. Values of convexity are in units of 1 divided by length (Wood, 1996).

point to faults and veins with higher clay contents and will be seen as areas of low electrical resistivity. Notably, the ring fault of the structural margin of the Silverton caldera is predicted to be electrically resistive in the Mineral Creek drainage, and generally more conductive along the drainage of the upper Animas River. This suggests that the ring structures associated with the upper Animas River are altered and likely clay filled, and may act as barriers to structurally controlled ground-water flow. The resistive ring structures found near the Mineral Creek drainage may also act as aquitards (a layer of rock or a geologic structure having low permeability that impedes ground-water flow) if these faults and mineralized veins are filled with quartz, as predicted by their electrical signature.

The result of the predictive modeling suggests that silicic mineralogy more commonly characterizes the faults and veins present in the watershed study area. Ground electromagnetic (EM) surveys conducted for this study in Placer Gulch (fig. 1) indicated high resistivity values over the mineralized veins. The predictive model also indicates that structures in this area are likely resistive, and therefore composed of silicic material. Figure 20 shows the location of the ground EM survey and known structures. Field reconnaissance has shown that silicic veins are common in the Placer Gulch area.

Magnetic Models

Magnetic Characteristics of Shallow Geologic Structures

The statistical methodology was used to evaluate whether the faults and veins have a characteristic magnetic signature as expressed by anomaly amplitude in the high-pass magnetic map (fig. 8). Weights were computed using the high-pass magnetic anomaly data layer and geologic structures data layer. Results revealed a bimodal magnetic signature indicating that faults and veins are most likely to occur over

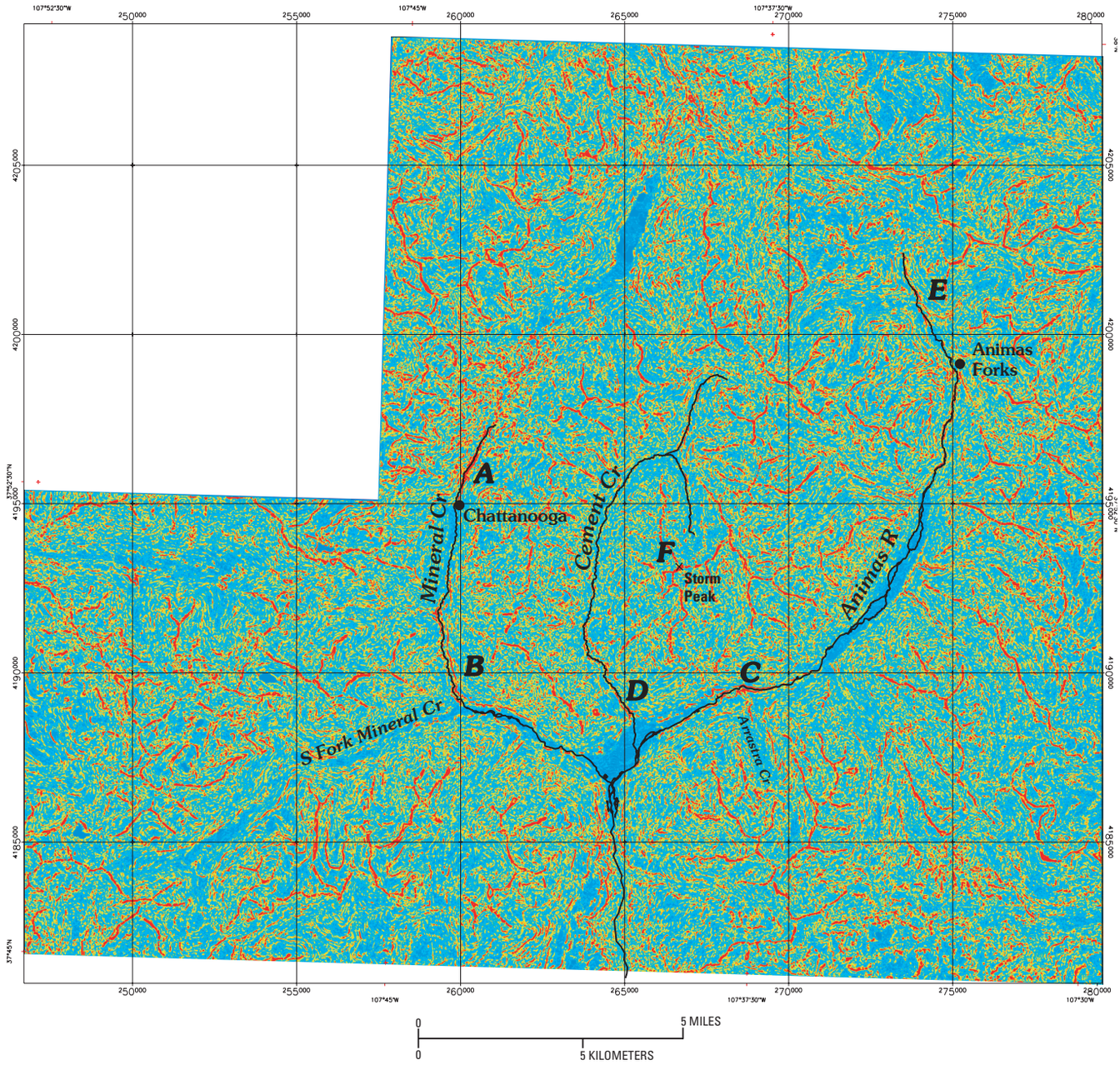

Figure 17. Profile convexity predictive model of geologic structures. Blue, lower probabilities (weights); red, higher probabilities; yellow, moderate. A–F, areas where stream channels and ridges have high probabilities of structural control.

very low amplitude magnetic anomalies and, to a lesser degree, over moderately high amplitude magnetic anomalies (fig. 21*A*). Initially, it may appear that there are more magnetic anomaly classes showing positive weights in the high magnetic anomaly range. However, most of the high magnetic value classes showing association with geologic structures occupy small areas. Most of these areas coincide with structures within the Sultan Mountain stock (Yager and Bove, this volume). In contrast, classes with high weights located within low magnetic anomaly classes occupy significantly more area in the overall magnetic anomaly grid. Consequently, low magnetic anomaly values better typify the magnetic signature of most of the faults and veins.

The horizontal gradient of the magnetic potential, calculated from the high-pass magnetic data, indicates a positive spatial association with steep magnetic gradients (fig. 21*B*). As discussed previously, magnetic gradients occur at boundaries between rocks with different magnetic properties. The steeper the gradient, the shallower the contact, or the greater the magnetic contrast between juxtaposed rock units.

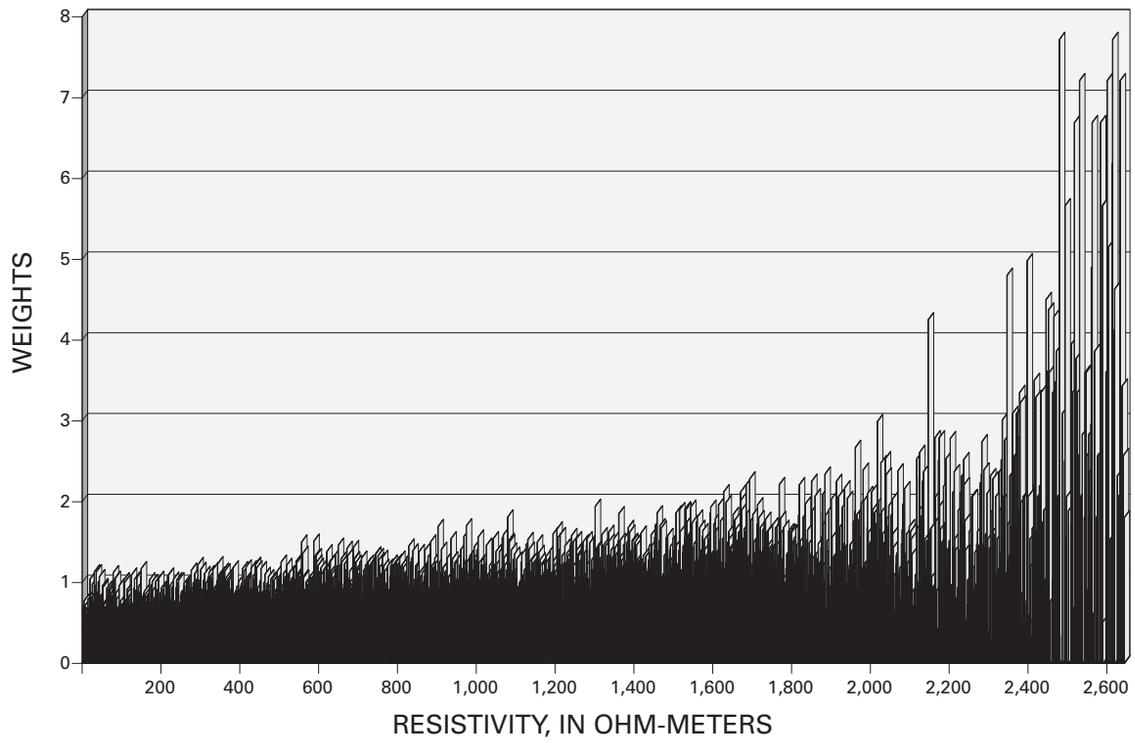

Figure 18. Weights of association of electrical resistivity with mapped structures.

The predictive model calculated from the weights of the high pass HGM (fig. 22) shows areas where structures are likely to occur near the surface based on the magnetic gradient magnitude. In many areas, mapped structures coincide with the highest probabilities (areas in red). The model also identifies permissive areas for structures. Examples of these areas are shown in figure 22 at (A) Anvil Mountain, (B) east of Ohio Peak, (C) southeast of Emery Peak, and (D) northeast of Howardsville.

Magnetic Characteristics of Deep Crust Geologic Structures

Magnetic anomalies related to deep crustal features, such as covered parts of the Silverton caldera, are difficult to discern in the RTP map (fig. 7) because of the influence of shallower magnetic sources, which tend to mask anomalies associated with deeper sources. However, the low-pass magnetic anomaly and the horizontal gradient magnitude (HGM) of the low-pass magnetic field (figs. 9 and 11, respectively) enhance magnetic anomalies associated with buried features and allow for an evaluation of which geologic structures exposed at the surface may continue from the shallow crust to deeper levels.

A visual comparison of the low-pass HGM with mapped geologic structures (fig. 11) shows many of the fault structures mapped at the surface correlate with deeper magnetic boundaries or sources. The statistical comparison (fig. 23) performed between faults and the HGM low-pass magnetic data supports the visual observations. Low to moderate magnetic gradients are associated with the locations of fault structures. The structural margin of the Silverton caldera coincides with moderately steep magnetic gradient maxima that, for the most part, lie outside the Animas River and Mineral Creek drainages. The pronounced magnetic boundary that parallels the southeast part of the Silverton caldera ring fault (fig. 11) is likely the magnetic expression of the structural margin of the older San Juan caldera. The southwestern part of the Eureka graben is characterized at depth by the pronounced magnetic anomaly low in figure 11 that reflects a large volume of nonmagnetic volcanic rock. The Ross Basin and Sunnyside faults are located over moderate amplitude HGMs. The magnetic boundary that coincides with the Ross Basin fault, however, continues in a northwest and southeast direction beyond its surface expression. The southeast HGM projection of the Ross Basin fault crosses the Eureka graben where it intersects the Toltec fault. The northwest HGM projection of the Ross Basin fault continues another 2 km beyond its mapped extent (fig. 11).

Some of the major fault structures not expressed magnetically at deeper levels include the Toltec and Bonita faults. Though the Toltec fault does not coincide with a deep crustal magnetic boundary, a parallel HGM trend is obvious to the southeast. The Bonita fault is not expressed magnetically at deeper crustal levels, but the points at which it intersects with the Ross Basin and Toltec faults are present magnetically as moderate amplitude HGM (fig. 11).

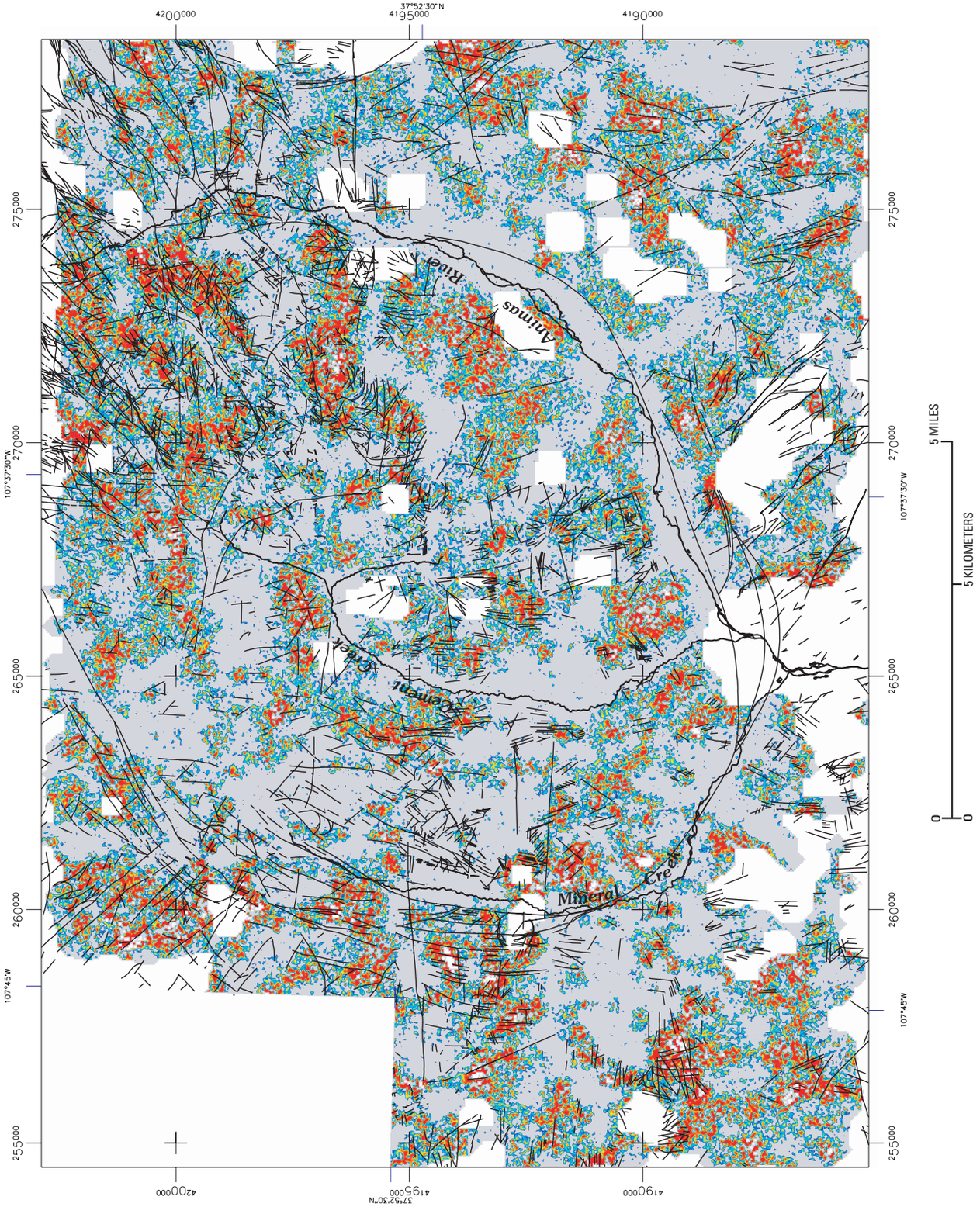

Figure 19. Electrical resistivity predictive model of geologic structures. Cooler colors, lower probabilities (weights); warmer colors, higher probabilities. White, areas of no data; gray, areas of no overlap.

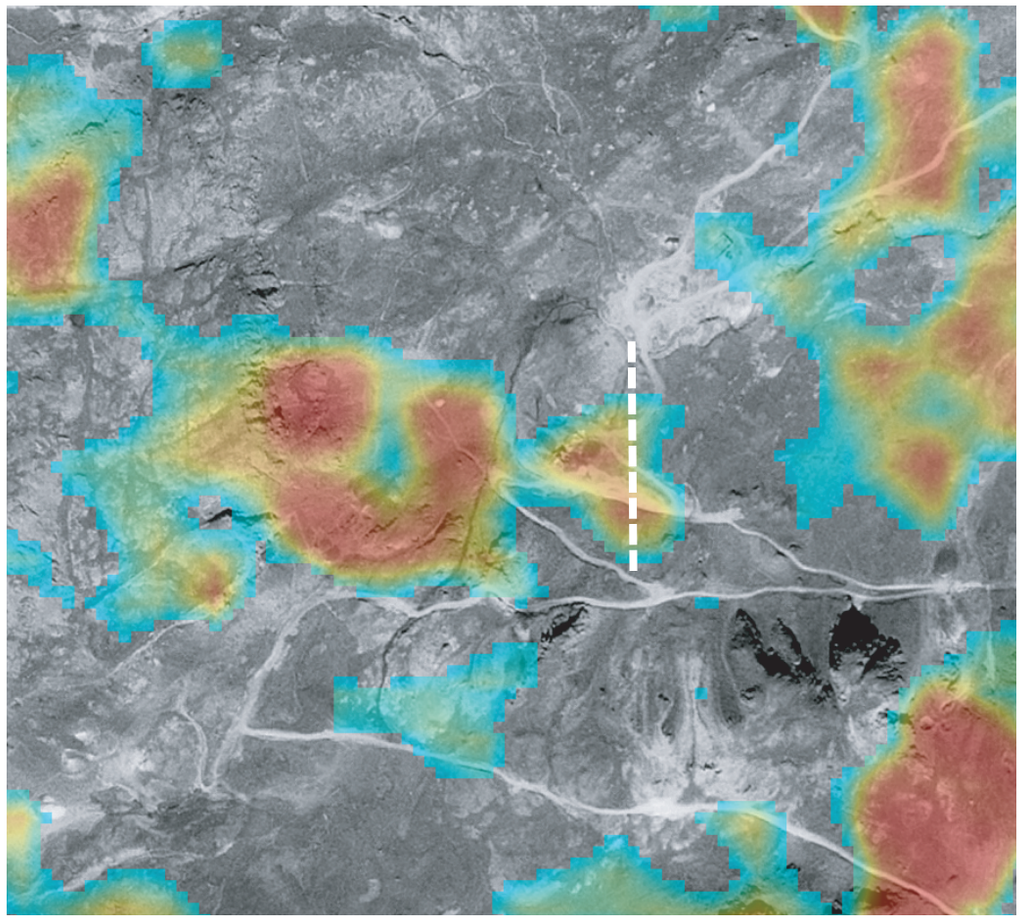

Figure 20. Predictive model of resistivity (left) showing location of ground electromagnetic (EM) survey (white dashed line) in Placer Gulch. Only probabilities greater than 1 are shown. Higher probabilities of structures are shown in red. Photo (right) shows example of silicic vein in Placer Gulch. Height of outcrop is approximately 25 m.

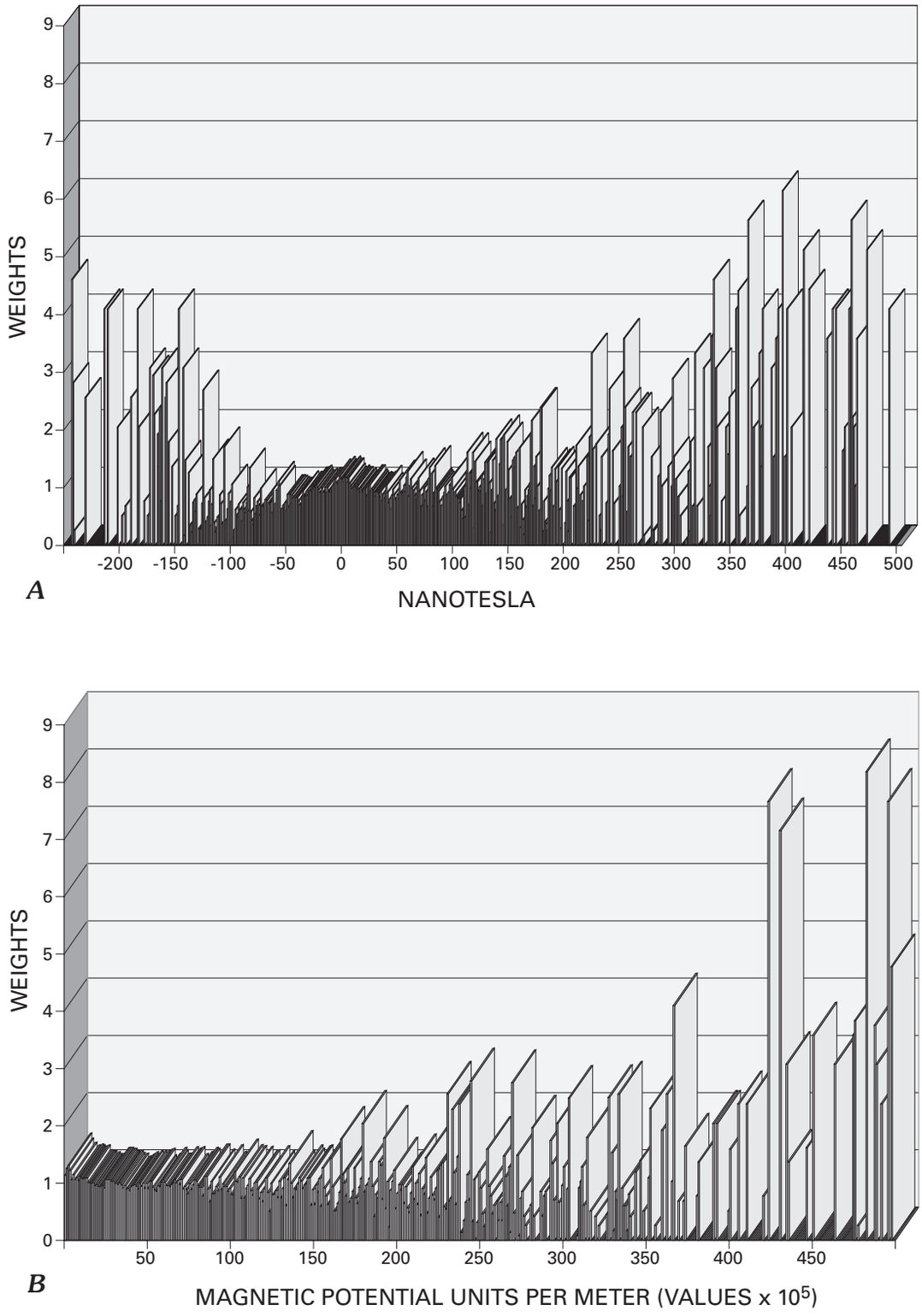

Figure 21. Calculated weights of *A*, magnetic high-pass filtered data, and *B*, high-pass filtered horizontal gradient magnitude (HGM) associations with geologic structure.

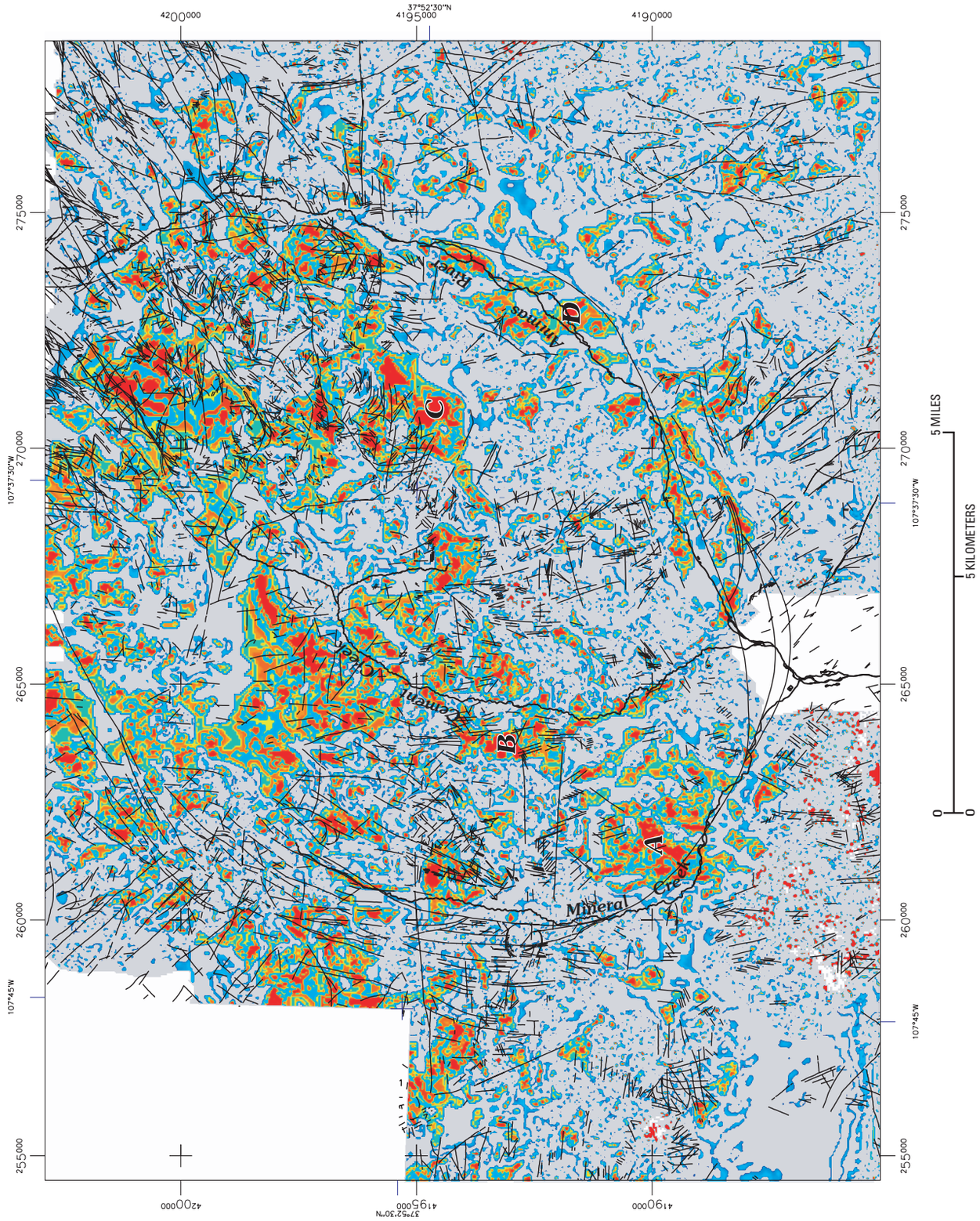

Figure 22. High-pass horizontal gradient magnitude (HGM) magnetics predictive model of geologic structures. Cooler colors, lower probabilities; warmer colors, higher probabilities. White, areas of no data. Examples of permissive areas for structures are shown at A, B, C, and D.

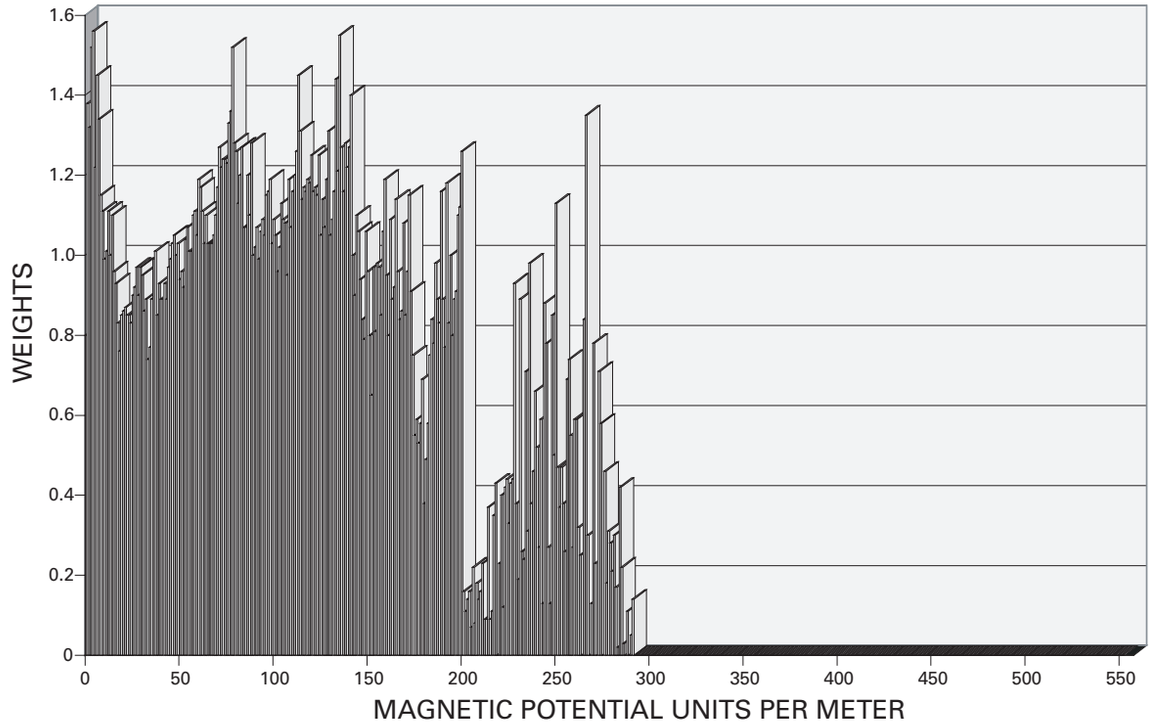

Figure 23. Calculated weights of geologic structure association with low-pass magnetic horizontal gradient magnitude (HGM).

In addition to the linear magnetic boundary that parallels the Toltec fault, other magnetic gradient trends are present that are parallel to either mapped structure or drainage trends. Two of the more interesting of these are the magnetic boundaries that parallel the semi-elliptical trend formed by Cement Creek and South Fork Cement Creek. Arcuate magnetic boundaries mimic this pattern to the south of the drainages. The concentric nature of these magnetic boundaries could be an expression of the resurgent doming that occurred in the formation of the nested Silverton and San Juan calderas (Luedke and Burbank, 2000).

Steepest magnetic gradients present in figure 11 coincide with the contact between the magnetic Tertiary Sultan Mountain stock and the surrounding, less magnetic country rock. The steep magnetic gradients that coincide with the edge of the Sultan Mountain stock are not reflected in the weights chart (fig. 23) because only fault structures were compared to the HGM of the low-pass magnetic data. The elongate HGM feature associated with the Sultan Mountain stock is a prominent element in figure 11, however, and marks a significant through-going geologic boundary. It therefore warrants some discussion. Comparison of the mapped outcrop of the Sultan Mountain stock (Yager and Bove, this volume, pl. 1), west of Silverton, with the HGM shows a close coincidence between the two features. This coincidence supports a nearly vertical sided geometry to a depth of at least 3 km. Other unnamed Tertiary stocks that occur within and near the periphery of the Silverton caldera are associated with the large semicircular to scalloped-shaped long-wavelength magnetic high that rings the Silverton caldera (fig. 9). Although their mapped extents do not have as close a coincidence with magnetic boundaries, most of the Tertiary stocks occur near parallel magnetization boundaries. Magnetic rock properties determined from samples of the Sultan Mountain stock and other unnamed Tertiary intrusions show them to possess some of the highest magnetic susceptibilities in the study area (Gettings and others, 1994). Consequently, the Tertiary plutons are a likely source for the arcuate magnetic high, and the continuous nature of this feature suggests that the plutons may be connected, forming a continuous mass at depth.

Mineralogic Models

The weights charts produced from comparison of mapped structure to AVIRIS mapped mineralogy are intended to provide a general characterization of mineralized faults and veins in terms of their acid-generating or acid-neutralizing potential (AGP, ANP). A limitation to the AVIRIS mineral maps and their relationship to structure is that in many parts of the study area the surface mineralogy is not exposed because of

vegetation cover or snow cover. Also, in some cases, structures may not have been mapped because they are covered with soil, alluvium, or talus.

The chart of weights of the AGP group minerals (fig. 24*A*) shows a random association of jarosite, goethite, and hematite to structures within the watershed. Structures are most likely to be associated with amorphous iron oxide and iron hydroxide minerals. This model would suggest that structures do not have a positive association with acid production based upon their mineralogic distribution. However, this does not preclude that there are structures that have provided discrete pathways for acidic and metal-rich waters.

The weights chart for the ANP group minerals (fig. 24*B*) indicates positive associations of epidote and chlorite, chlorite, and mixtures of chlorite, muscovite and calcite, to mapped structure. This is consistent with the pervasive occurrence of propylitically altered rocks in the study area. The random association of the "pure" end members of calcite and epidote suggests that these minerals occur primarily in mixtures with the other minerals of the propylitic alteration assemblage. Calcite is reported to have only 1 percent abundance in veins near the Sunnyside mine workings (Casadevall and Ohmoto, 1977), so that calcite would not be expected to have a positive association with structure.

Model Validation

Validation, or verification of results, is a fundamental component of any predictive modeling investigation (Chung and Shaw, 1999). The validity of the models produced in this study was analyzed in several ways. First, we examined the stability of the models by random alteration of the reference area data. Second, the topographic and geophysical models were compared to two geologic cross sections. Finally, we used the predictive maps to guide field investigations of structures expressed at the surface.

Model Stability

The stability of the models (also referred to as sensitivity by Lee and others, 2001) is an indication of how dependent the success rate of spatial association is between an evidential layer and a prototype area with respect to changes in the definition of the reference area (in this case the mapped faults and veins). To test the stability of the models, we compared the various evidential layers (profile convexity, resistivity, and magnetics) to the prototype layer which was randomly decimated to 50 percent of the original population of structures. Probability ratios were calculated using the decimated reference area, and weights charts were prepared.

Comparison of the weights charts (fig. 25) shows that the models produced from the decimated reference data layer have similar distribution characteristics to the models calculated from the original reference data layer. This indicates that the models are not dependent on the definition of the reference layer, and are therefore considered stable. An exception is seen in the high-pass filtered magnetic models in the high amplitude anomaly range (≈300–500 nT). Weights tend to be higher in the model produced from the decimated reference layer and there is no overlap in this model in the ≈470–500 nT range. However, as previously discussed, the overlap area of structures with high-pass magnetic data in this range tends to be smaller than in the low amplitude anomaly range. Therefore, the low amplitude range better typifies the magnetic signature of most of the faults and veins.

The data layers of ANP and AGP minerals were not modeled using the decimated reference data layer because of the relatively sparse density of AVIRIS mineralogic data coverage. The extent to which the mineralogy is obscured can be seen in figure 14. In fact, 71 percent of the study area is covered by vegetation and snow, and 66 percent of the mapped structures are covered.

Comparison of Geophysical and Profile Convexity Profiles to Geologic Cross Sections

A second aspect to the model validation includes a comparison of predicted locations of geologic structures to mapped structures in profile. Geologic cross sections (locations shown on map, fig. 1) in the western and southeastern parts of the study area are available from geologic mapping of the Silverton and Howardsville 7.5-minute quadrangles (Luedke and Burbank, 2000). Data that co-registered with the cross section locations were extracted from the high-pass magnetic, 4,310 Hz resistivity, and profile convexity grids. The north profile, A–A' (fig. 26), runs from west to east and begins north of Middle Fork Mineral Creek, crosses south of Ohio Peak, and ends southwest of Storm Peak. The profile is entirely within the Silverton caldera. The south profile, B–B' (fig. 27), begins at the southern ridge of Storm Peak, continues in a southeasterly direction across the upper Animas River to Hazelton Mountain, and ends on the north ridge of Whitehead Peak. In terms of geological extent, this profile begins in the Silverton caldera, crosses its structural margin, and continues beyond the outer rim of the older San Juan caldera.

Weights of predicted locations of geologic structures from the various data layer models are shown as red bars below the corresponding geophysical or profile convexity profiles. The variable bar heights indicate the *relative* strength of positive spatial associations, with only weights greater than 1 shown. Therefore, the values on the vertical axis on all the cross sections correspond only to the values of magnetics (nT), resistivity (ohm-m), profile convexity (L^{-1}), or elevation (m). Small squares on the geophysical or profile convexity profiles indicate the projection of a mapped mineralized fault or vein (red), an andesitic dike (green), or a fault (black) onto the profile for reference.

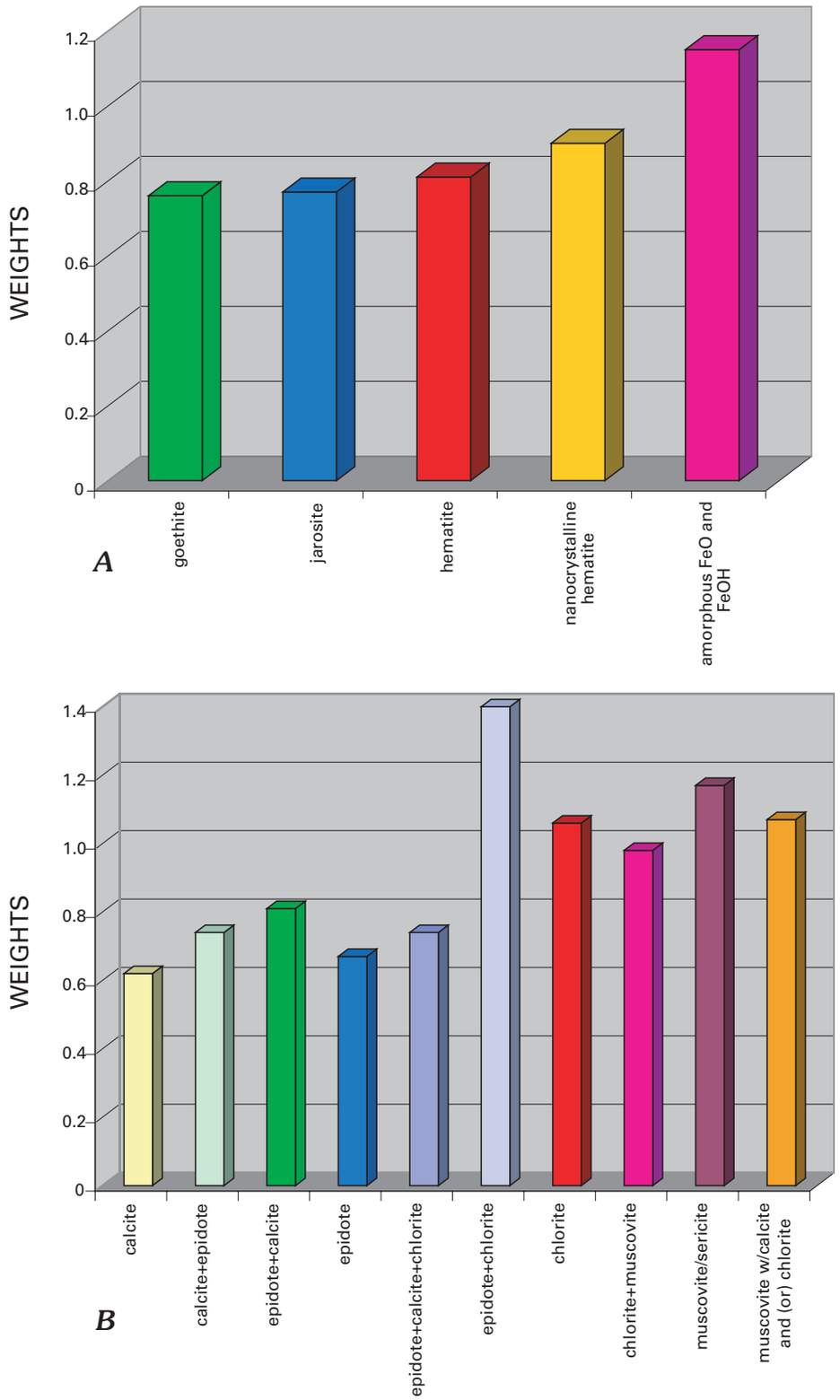

Figure 24. Calculated weights of geologic structure association with *A*, acid-generating potential (AGP), and *B*, acid-neutralizing potential (ANP) group minerals based on mineralogic analysis of AVIRIS data.

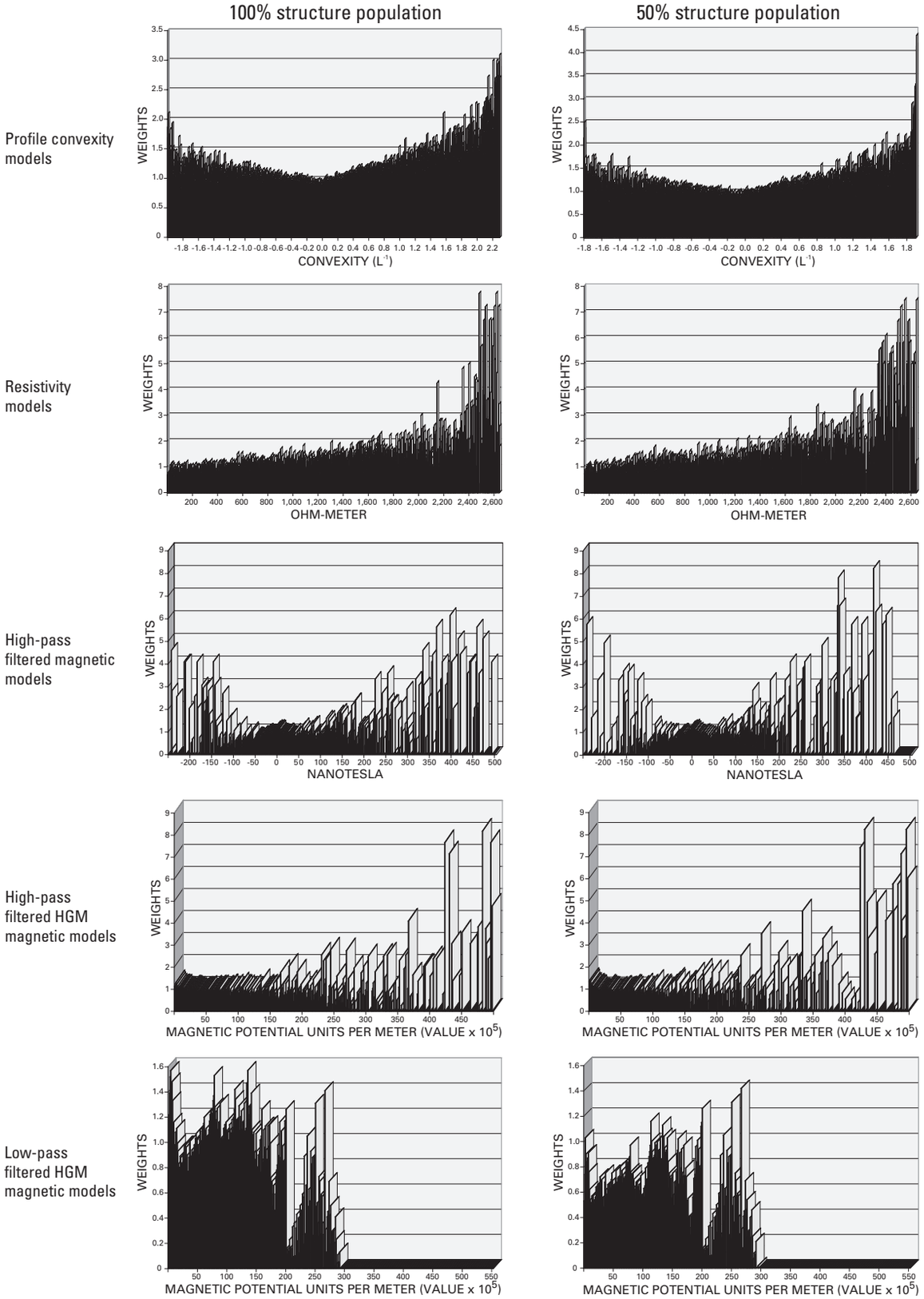

Figure 25. Comparison of predictive models for verification. Models in left column were produced using 100 percent of mapped structures; models in right column were produced using a randomly decimated population of 50 percent of mapped structures.

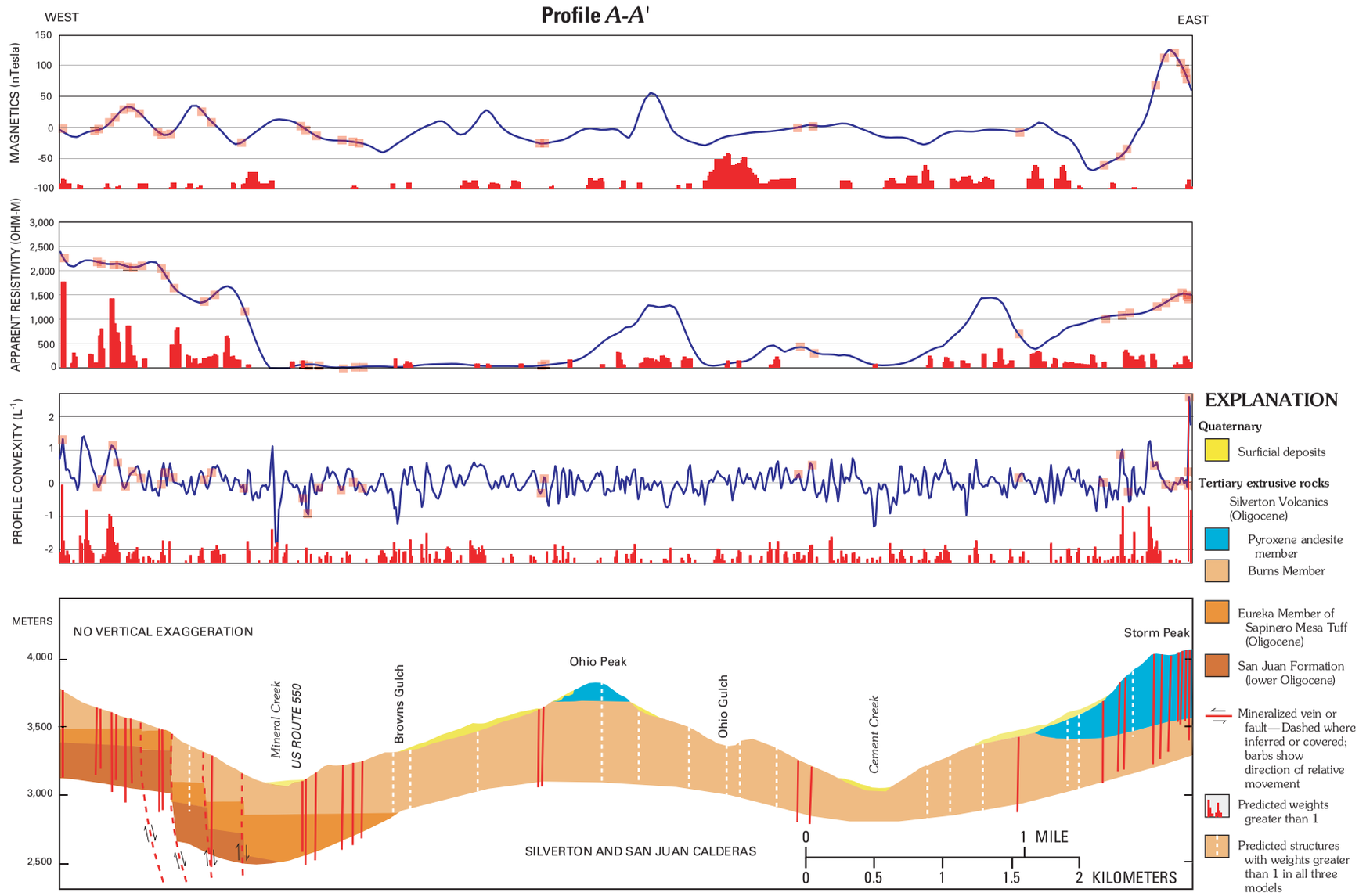

Figure 26. High-pass magnetic, 4,310 Hz apparent resistivity, and profile convexity profiles over geologic cross section (Luedke and Burbank, 2000). Boxes on profiles map locations of mineralized veins or faults (red). Locations of predicted structures from modeling are shown as red bar charts at bottom of related profile. Predicted structures with coincident locations in all three models are shown as white dashed lines. Location of section is shown on figure 1.

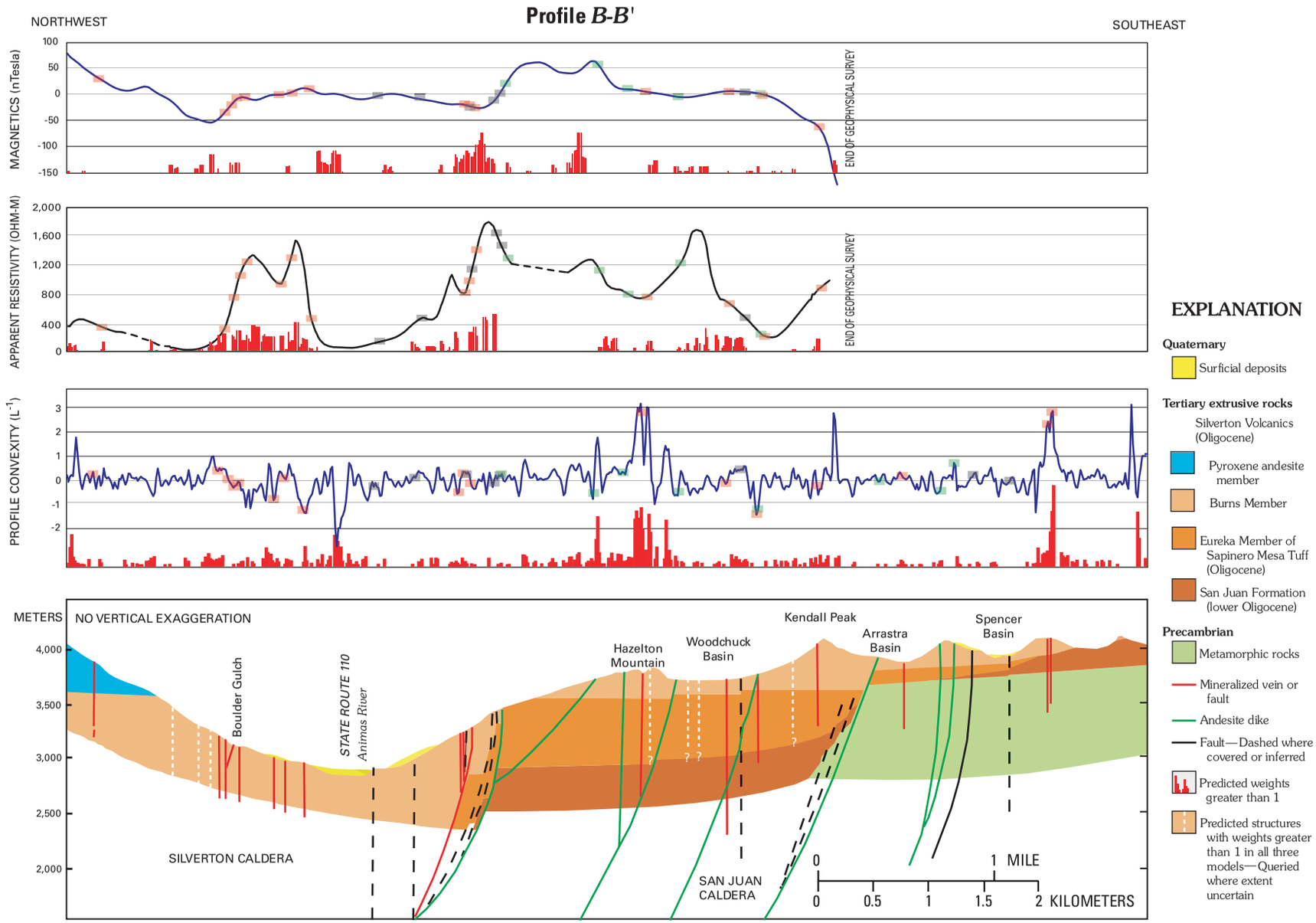

Figure 27. High-pass magnetic, 4,310 Hz apparent resistivity, and profile convexity profiles over geologic cross section (Luedke and Burbank, 2000). Boxes on profiles map locations of mineralized veins or faults (red), andesite dikes (green), and faults (black). Locations of predicted structures from modeling are shown as red bar charts at bottom of related profile. Predicted structures with coincident locations in all three models are shown as white dashed lines. Location of section is shown on figure 1.

In general, for both profiles, the majority of predicted locations of faults and veins lie along geophysical anomaly gradients and not on resistivity or magnetic anomaly peaks. Additionally, predicted locations tend to intersect the gradients of resistivity anomalies with moderately high values. Strongest spatial associations in the resistivity model (fig. 18) are defined by higher weights within a moderately high to high resistivity value range. Where high resistivity values are associated with structures, the high values tend to be due to infilling of structures with silicic material. Less common but still present are lower model weights, barely above a probability ratio of 1, which point to geologic structures located in electrically conductive (low resistivity) rock and soil material such as clays.

The predicted locations of geologic structures along the magnetic anomaly profiles share a similarity with those of the resistivity data in that predicted locations of faults and veins occur along magnetic gradients. However, in contrast to the resistivity data, geologic structures occur over a wide range of magnetic anomaly values indicating that geologic structures occur in rocks with a wide range of rock magnetizations.

The profile convexity model predicts the occurrence of structures primarily in areas of moderate to extreme convexity. A general observation of the convexity models in both cross sections indicates that an overabundance of structures seems to have been predicted. Note, however, that many of the weights shown have values just slightly greater than 1, and therefore should be considered significant only where groupings of higher weights occur.

On geologic cross section A–A' (fig. 26), the majority of mapped mineralized veins and faults are located west of Mineral Creek and are part of a fault zone that defines the structural margins of the San Juan and Silverton calderas, which are interpreted to be more or less coincident here. The caldera margins are characterized by faults and fractures that have provided ample pathways for the emplacement of intrusive igneous material and mineralized fluids (Luedke and Burbank, 2000).

All three models show a number of predicted structures coincident with mapped structures (table 1). Between the west end of profile A–A' and Mineral Creek, there are 14 mapped mineralized veins. Out of the 14, the magnetic model located 8 (57 percent), the resistivity model located 12 (86 percent), and the profile convexity located 7 (50 percent). High weights in association with high resistivities and positive convexities suggest that this area is extensively silicified from the intense veining. The magnetic anomaly highs over this area, however, suggest that the nonmagnetic character of the silicification is relatively thin (50 m or less). The magnetic signature likely relates to the greater volume of San Juan Formation that underlies the Oligocene Eureka Member of the Sapinero Mesa Tuff and Burns Member of the Silverton Volcanics. Rock magnetic property measurements on rocks within the Silverton caldera show the San Juan Formation volcanic rocks to be significantly more magnetic than those of the Eureka or Burns Members (Gettings and others, 1994). Along the caldera margin, segments of the San Juan Formation have been uplifted to shallower levels in the fault blocks along the caldera margin, which best explains the presence of magnetic highs in this area of profile A–A'.

A significant drop in resistivity occurs at Mineral Creek and continues east along profile A–A' across Browns Gulch to Ohio Peak. The convexity profile also drops significantly at Mineral Creek, which would suggest that, at least along this reach, the stream is structurally controlled. The extreme negative convexity and low resistivity values are characteristic of areas where alteration is associated with zones of crustal weakness. This section of the profile is entirely within the Silverton and San Juan calderas and mapped as the Burns Member of the Silverton Volcanics blanketed with a thin veneer of Quaternary surficial deposits. In map view, the resistivity low (fig. 13) coincides with a triangular magnetic anomaly low (fig. 8). A slight increase in resistivity and magnetic anomaly amplitudes occurs within the center of the lows along the west flank of Ohio Peak. In map view, the subtle rise in resistivity and magnetic values within the larger resistivity and magnetic lows is suggestive of an intrusion at depth that has extensively altered the surrounding country rock. Eight mapped structures are present in this area of intense alteration, and the magnetic and resistivity models did a poor job of predicting the exact locations of this set of faults (13 and 25 percent of the structures were predicted, respectively). Much of this part of A–A', especially between Browns Gulch and Ohio Peak, is covered with surficial deposits. The resistivity model predicts structures within this more electrically conductive area, but not in association with mapped structures. Because the modeling is based on an area calculation, we suggest that the silica-rich structures are more common (cover a larger area) in the study than structures filled with clay-rich material, such as would be produced in areas with intense alteration.

The magnetic and resistivity anomaly highs that occur to the east of Ohio Peak are offset from the topographic peak. The offset from the mountain top may be due to the presence of more pyroxene andesite in the subsurface between Ohio Peak and Ohio Gulch. The pyroxene andesite is one of the most magnetic and resistive rock types within the study area.

The magnetic, resistivity, and profile convexity models would all suggest that Ohio Gulch is structurally controlled based on the presence of predicted structures in all three models. Highest weights in the magnetic model for profile A–A' occur at Ohio Gulch. Geophysically, Ohio Gulch is characterized by low magnetizations and resistivities, suggesting a structure or structures likely dominated by clay rather than silica mineralogy. Topographically, structures are indicated in this area by the negative convexity.

Table 1. Numerical comparison of geologically mapped structure locations along profiles *A–A'* (fig. 26) and *B–B'* (fig. 27) to locations of geologic structures predicted by high-pass magnetic, 4,310 Hz resistivity, and profile convexity models.

		Number of mapped structures (Luedke and Burbank, 1990)	Predicted number of structures (percent predicted out of total structures)		
			High-pass magnetic	4,310 Hz resistivity	Profile convexity
Profile *A–A'*	West end of profile to Mineral Creek	14	8 (57%)	12 (86%)	7 (50%)
	Mineral Creek to Ohio Gulch	8	1 (13%)	2 (25%)	2 (25%)
	Ohio Gulch to Storm Peak	13	4 (31%)	8 (62%)	10 (77%)
	TOTAL Profile *A–A'*	**35**	**13 (37%)**	**22 (63%)**	**19 (54%)**
Profile *B–B'*	NW end of profile to Animas River	8	3 (37%)	7 (87%)	6 (75%)
	Animas River to Hazelton Mtn	12	6 (50%)	8 (67%)	10 (83%)
	Hazelton Mtn to Kendall Peak	7	5 (71%)	5 (71%)	5 (71%)
	TOTAL Profile *B–B'*	**27**	**14 (52%)**	**20 (74%)**	**21 (78%)**

Storm Peak is covered with the same pyroxene andesite rock as at Ohio Peak, and magnetic and resistivity anomaly highs with large amplitudes occur here as well. Thirteen structures are mapped between Ohio Gulch and Storm Peak, with 10 of the 13 mineralized veins located within the pyroxene andesite of Storm Peak. As is the case for most of the study area, the resistivity model predicted geologic structures within the moderately high value resistivity range that occurs over Storm Peak. Of the 10 mineralized veins that occur within the pyroxene andesite, the resistivity model predicted 9, or 90 percent. The magnetic data predicted only 50 percent. Apparently, the pyroxene andesite at Storm Peak is fairly homogeneous in its magnetic properties and, although fractured, does not possess enough magnetization contrast within the fractures to produce variations in the magnetic anomaly.

Profile B–B' (fig. 27) extends for a distance of approximately 9 km, with coincident airborne geophysical data available for the northwesternmost 6 km. Four different types of geologic structures are mapped along the profile, including mineralized veins, faults, andesitic dikes, and nonmineralized faults.

From the northwest end of the profile to the Animas River, the profile is entirely within the Silverton caldera. One of the most pronounced features within this profile segment is the resistivity high occurring over Boulder Gulch. The resistivity model predicted 87 percent (table 1) of the mapped mineralized veins in this segment, with the distinct resistivity high likely due to intense silicic veining. The magnetic signature here is also consistent with a broad area containing a silicic mineralogy, as evidenced by magnetic anomaly values near zero. However, in terms of predicting the individual structures, the magnetic model did a poor job, only predicting 37 percent of the mineralized vein locations. The low likelihood of structures in the magnetic model coincides with the lack of pronounced magnetic gradients, as would be expected over an area with a homogeneous magnetic mineralogy. The profile convexity model predicted 75 percent of the mapped

structures in Boulder Gulch, and the model indicates that structures have both positive and negative convexity values. Notably, the Animas River is marked by an extreme negative convexity and low resistivity analogous to that seen in profile A–A' near Mineral Creek, suggesting a similar altered environment.

The contact between the Silverton and San Juan calderas is located between the Animas River and Hazelton Mountain and marked by a diversity of geologic structure types. The magnetic, resistivity, and profile convexity models did well predicting the zone of geologic structures marking this contact (table 1). This section of the profile is characterized by steep geophysical gradients, high resistivity, and low magnetizations.

Once the caldera contact is crossed, the magnetic anomaly amplitude increases and likely is the result of the more magnetic mineralogy of the San Juan Formation. Plutonic rocks similar to those exposed within the Sultan Mountain stock may be present in the subsurface. The magnetic high is part of a ring-shaped high that is a pronounced feature in the magnetic maps (figs. 7, 8, and 9) and is connected to the west with the magnetic Sultan Mountain stock. The northwest-dipping mapped andesite dike approximately 500 m northwest of Hazelton Mountain is shown in the profiles to be erosionally and electrically resistive, and magnetic. These characteristics are consistent with the properties of other andesite dikes in the study area.

Hazelton Mountain is characterized topographically by extreme positive convexity. Near the summit the convexity decreases substantially in apparent correlation with a mapped structure. The geophysical profiles indicate that this structure is relatively nonresistive and nonmagnetic, and therefore, is likely altered.

In Woodchuck Basin (fig. 27), the mapped structures are characterized by somewhat positive to significantly negative convexity, and they are nonresistive (conductive) and nonmagnetic. As in other cases, these characteristics are typical of altered and likely clay filled structures.

Near the end of the geophysical profiles the resistivity begins to increase and the magnetic profile goes sharply negative. This is interpreted as the geophysical response to Precambrian metamorphic rocks mapped at depth. However, because the profiles here are at the limit of the geophysical survey, edge effects resulting from filtering of the data may introduce inaccuracies that should be considered in the interpretation.

A final utility of the profiles comparing the topographic and geophysical data and predictive models to mapped structures was to determine where predicted structures with weights greater than 1 had coincident occurrence in all three models. We assumed that where the three models all predict structures, locations are identified where previously unmapped structures may exist. In figure 26 and figure 27 the predicted structures are shown as white dashed lines on the geologic cross sections.

For profile A–A', 16 "structures," or locations of coincidence, were identified. Notably, Browns Gulch, Ohio Peak, and Ohio Gulch are favorably associated with predicted structures. A total of 35 structures (table 1) are mapped on this profile, which means that 46 percent more mineralized and nonmineralized faults and veins are predicted. Profile B–B' shows seven predicted structures, or 26 percent more than are mapped in the cross section.

Field Verification

In practice, verification by direct observation in the field or by comparison to known data, such as geologic maps, can be the most critical test of a predictive model. As previously discussed, the profile convexity predictive model map (fig. 17) shows examples of coincidence of predicted structures with stream channels or ridges. These examples are typical of the agreement between the topographic model and known mapped structures throughout the study area.

The ground EM survey conducted in Placer Gulch, as previously discussed, is an example of agreement between the resistivity model and direct field investigation (fig. 20). The model predicts that structures in this area should be electrically resistive, and the results of the ground surveys support this prediction.

During the fall of 2003, field investigations were guided in part by the predictive models of topography, resistivity, and magnetics. Areas of interest included Boulder Gulch and the South Fork Cement Creek (fig. 1). Figure 28 shows an example in Boulder Gulch of a mapped silicified vein that, as indicated by the airborne geophysical data, is in an area that is moderately resistive and nonmagnetic. The profile convexity model predicts that a structure should exist in this location based on the topographic characteristics. Although less precise in location, the resistivity model indicates that the mapped vein is in an area favorable for electrically resistive structures. The high-pass HGM magnetic model predicts that the mapped structure is near a steep magnetic gradient, suggesting a significant difference in the magnetic properties of juxtaposed rock types.

Figure 29 shows an area near the headwaters of South Fork Cement Creek where alteration (vein-related quartz-sericite-pyrite; Bove and others, this volume) and subsequent erosion have occurred. Notably, the profile convexity model predicts a structure in this location. However, the geologic map of faults and veins (Yager and Bove, 2002; Yager and Bove, this volume, pl. 1) does not show a mapped structure associated with the gully. The resistivity map indicates that this altered and eroded zone is electrically nonresistive (conductive), which suggests the presence of wet clays or high dissolved solids in surface or ground water. The resistivity and high-pass HGM magnetic models show the area to be moderately permissive for structures based on the electromagnetic and magnetic gradient characteristics.

Silicified vein (shown at arrow) and adjacent fault in west-trending tributary of Boulder Gulch (view looking west). Height of outcrop at arrow approximately 2 m.

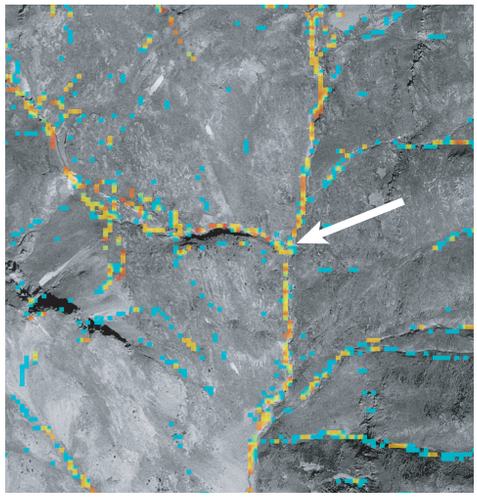

Profile convexity model and location of example silicified vein (shown at arrow). Probabilities are shown as blue (lowest) to red (highest).

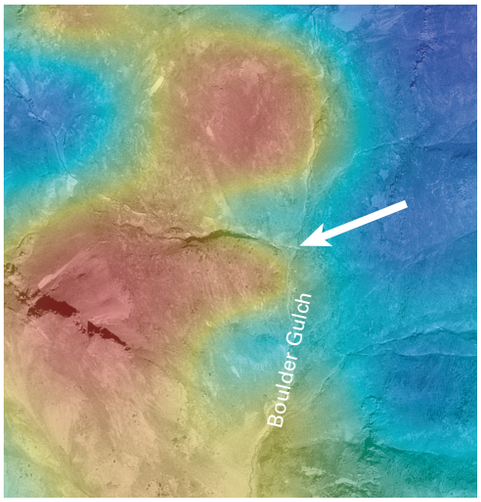

Resistivity map. Resistivity values are shown as blue (lowest) to red (highest).

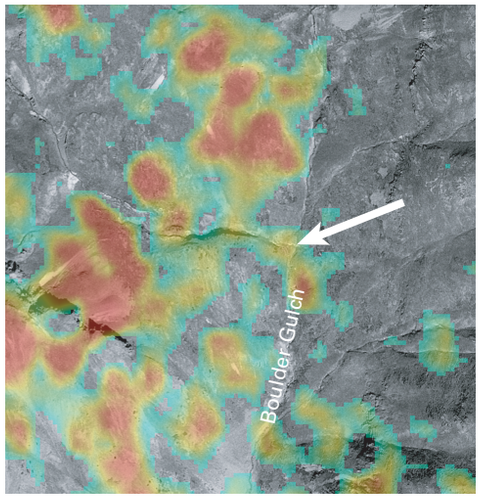

Resistivity model. Probabilities are shown as blue (lowest) to red (highest).

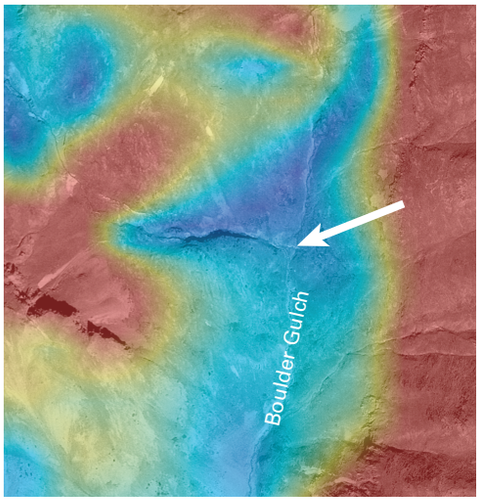

High-pass horizontal gradient magnitude (HGM) magnetics map. Gradients are shown as blue (lowest) to red (steepest).

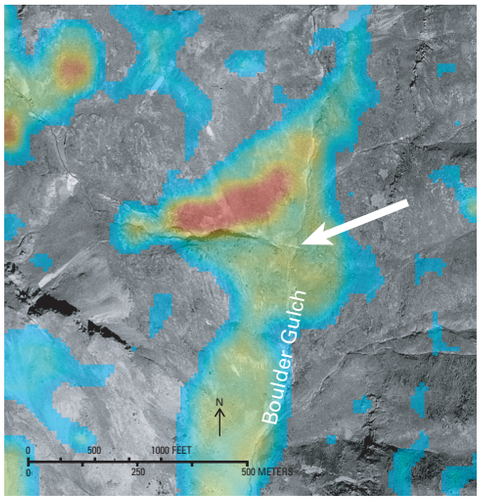

High-pass horizontal gradient magnitude (HGM) magnetics model. Higher probabilities are shown as blue (lowest) to red (highest).

Figure 28. Comparison of profile convexity, resistivity, and magnetic models and maps to a silicified vein in Boulder Gulch. Location of the vein, approximately 900 m west of Macomber Peak (fig. 1) and shown in upper left photograph, is indicated on the ground by white arrows on the maps.

View looking west-southwest of altered and eroded zone near South Fork Cement Creek. Man for scale in foreground.

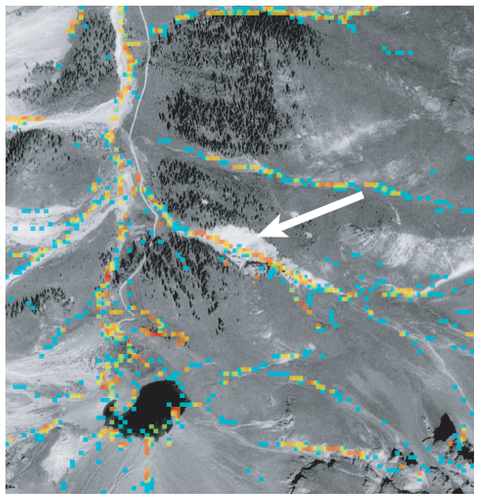

Profile convexity model and location of altered zone (shown at arrow). Probabilities are shown as blue (lowest) to red (highest).

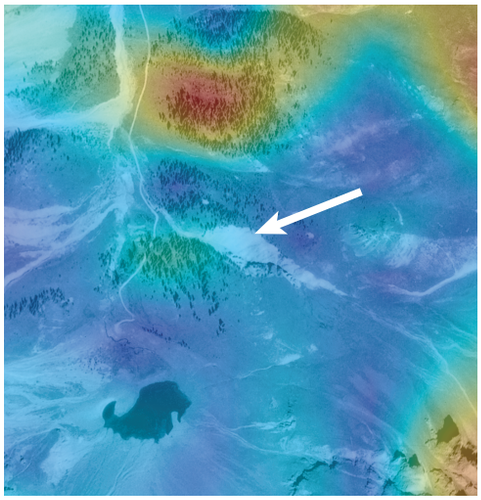

Resistivity map. Resistivity values are shown as blue (lowest) to red (highest).

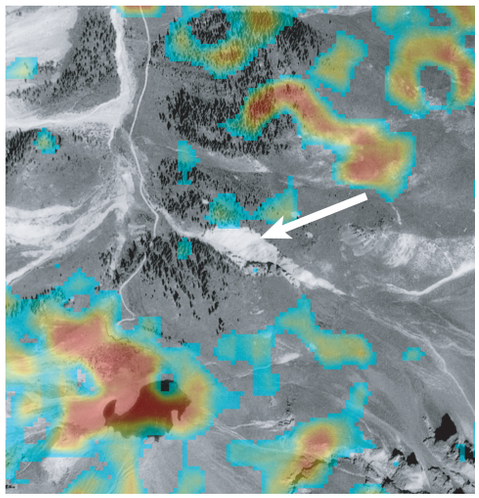

Resistivity model. Probabilities are shown as blue (lowest) to red (highest).

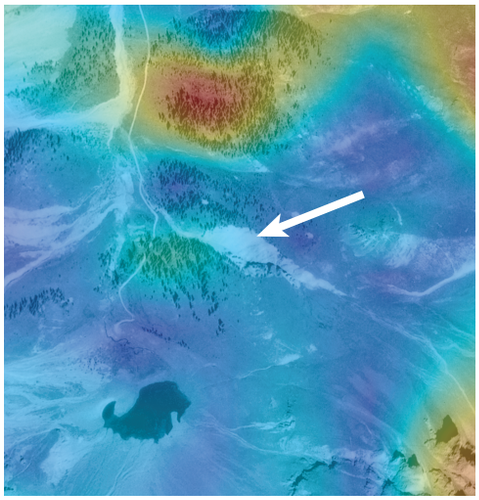

High-pass horizontal gradient magnitude (HGM) magnetics map. Gradients are shown as blue (lowest) to red (steepest).

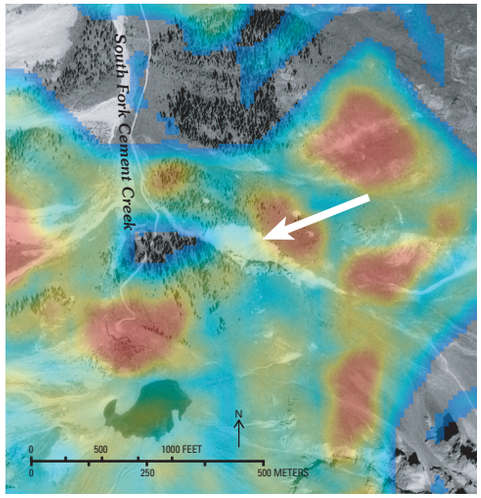

High-pass horizontal gradient magnitude (HGM) magnetics model. Higher probabilities are shown as blue (lowest) to red (highest).

Figure 29. Comparison of profile convexity, resistivity, and magnetic models and maps to an altered and eroded zone near the headwaters of South Fork Cement Creek. Location of the zone, shown in upper left photograph, is indicated on the ground by white arrows in the maps.

Conclusions and Discussion

This investigation was conducted to define and analyze the topographic, geophysical, and mineralogical characteristics of faults and veins within the study area. This information was used to predict permissive areas for unmapped geologic structures in the watershed. Topographic, geophysical, and mineralogical attributes were quantified for geologic structures, and the statistical method employed identified target areas for further investigation. In map form, the predictive models showing high probabilities accurately locate many known structures. More interestingly, the models suggest structures in areas where structures had not been previously mapped. Many of the permissive areas lie in places of restricted access, limited outcrop, and thick alluvial, soil, or vegetation cover.

Topographically, structures are characterized by erosionally resistant and likely silicified ridgelines, or as eroded and incised channels and valleys. The predictive model of structure derived from the topographic criteria identifies multiple areas where faults and veins extend beyond their previously mapped extent, or where unmapped structures may occur.

The planimetric orientation of electrical resistivity gradients identifies a prominent east-west orientation that correlates with one trend of unmapped structures. In terms of structurally controlled ground-water flow, faults and veins of this orientation would be least likely to provide flow paths. The resistive geophysical signature suggests that these structures are quartz filled and extend to a depth of at least 60 m. In areas where quartz-filled structures are fractured, secondary permeability may be considerable.

Magnetically, the faults and veins are characterized by either extreme low magnetizations or moderately high magnetizations, and moderately steep magnetic gradients. Magnetization boundaries associated with rocks at depths exceeding 1 km identify surface structures that may provide connectivity between the topographic surface and deep crust. Buried crustal boundaries not mapped at the surface are suggested by the magnetic data. Faults and veins are characterized by moderately high electrical resistivities and may point to more silica-rich phases within the Silverton Volcanics. The predictive model calculated from the electrical resistivity characteristics of structures identifies areas where faults and veins are resistive at depth, and as previously discussed, least likely to be structurally controlled ground-water conduits, except where significantly fractured.

Based on the results of the AVIRIS analysis, the mineralogical character of structures in terms of their acid-generating or acid-neutralizing potential suggests a random association with acid production resulting from the weathering of pyrite. Structures are most likely to occur in propylitically altered areas, and therefore are associated with rocks with the highest acid-neutralizing potential.

The predictive models presented here could be used to guide further geologic mapping and investigation, incorporated in hydrologic applications, or considered in remediation planning. The implication that significantly more mineralized and nonmineralized faults and veins (approximately 36 percent on average) may exist in the watershed than previously mapped might be important in terms of estimating fracture permeability that would be included in ground-water modeling efforts.

The methods and approaches employed in this study can be applied to other watersheds with similar structural and volcanic regimes containing acid-generating historical mines or source rocks. Further investigations may benefit from integration of the topographic, geophysical, and mineralogical characterization of structures presented here, with geochemical and geologic analysis to identify discrete ground-water flow paths and structurally controlled inflows to streams.

References Cited

Baranov, Vladimir, 1957, A new method for interpretation of aeromagnetic maps—Pseudogravity anomalies: Geophysics, v. 22, p. 359–383.

Bath, G.D., 1968, Aeromagnetic anomalies related to remanent magnetism in volcanic rock, Nevada Test Site: Geological Society of America Memoir 110, p. 135–146.

Blakely, R.J., 1995, Potential theory in gravity and magnetic applications: New York, Cambridge University Press, 441 p.

Burbank, W.S., 1933, Vein systems of the Arrastra basin and regional geologic structure in the Silverton and Telluride quadrangles, Colorado: Colorado Scientific Society Proceedings, v. 13, 214 p.

Burbank, W.S., and Luedke, R.G., 1964, Geology of the Ironton quadrangle, Colorado: U.S. Geological Survey Geologic Quadrangle Map GQ–0291.

Burbank, W.S., and Luedke, R.G. 1969, Geology and ore deposits of the Eureka and adjoining districts, San Juan Mountains, Colorado: U.S. Geological Survey Professional Paper 535, 73 p.

Casadevall, Thomas, and Ohmoto, Hiroshi, 1977, Sunnyside mine, Eureka mining district, San Juan county, Colorado—Geochemistry of gold and base metal ore deposition in a volcanic environment: Economic Geology, v. 92, p. 1285–1320.

Chung, C.F., and Shaw, J.M., 1999, Quantitative prediction models for landslide hazard assessment: Geological Survey of Canada Open File 3692, 1 sheet.

Church, S.E., Fey, D.L., and Blair, Robert, 2000, Pre-mining bed sediment geochemical baseline in the Animas River watershed, southwestern Colorado, *in* ICARD 2000; Proceedings of the Fifth International Conference on Acid Rock Drainage, Volume 1: Society for Mining, Metallurgy, and Exploration, Inc., p. 499–512.

Cordell, Lindrith, and Grauch, V.J.S., 1985, Mapping basement magnetization zones from aeromagnetic data in the San Juan basin, New Mexico, *in* Hinze, W.J., ed., The utility of regional gravity and magnetic anomaly maps: Society of Exploration Geophysicists, p. 181–197.

Dalton, J.B., Bove, D.J., Mladinich, C.S., and Rockwell, B.W., 2002, Spectral classification of similar materials using the USGS Tetracorder algorithm—The calcite-epidote-chlorite problem, *in* Green, R.O., ed., Summaries of the 10th Annual JPL Airborne Earth Science Workshop: Pasadena, Calif., JPL Publication 02–1, Jet Propulsion Laboratory, p. 93–103.

Desborough, G.A., Briggs, P.H., and Mazza, Nilah, 1998, Chemical and mineralogical characteristics and acid-neutralizing potential of fresh and altered rocks and soils of the Boulder River headwaters in Basin and Cataract Creeks of northern Jefferson County, Montana: U.S. Geological Survey Open-File Report 98–40, 21 p.

Desborough, G.A., and Yager, D.B., 2000, Acid-neutralizing potential of igneous bedrocks in the Animas River headwaters, San Juan County, Colorado: U.S. Geological Survey Open-File Report 00–0165, 14 p.

Fraser, D.C., 1978, Resistivity mapping with an airborne multicoil electromagnetic system: Geophysics, v. 43, no. 1, p. 144–172.

Gettings, M.E., Fisher, F.S., Gettings, P.E., and Luedke, R.G., 1994, Some magnetic properties of rocks from the Silverton Caldera area, Western San Juan Mountains, Colorado: U.S. Geological Survey Open-File Report 94–291, 28 p.

Grauch, V.J.S., 1988, Statistical evaluation of linear trends in a compilation of aeromagnetic data from the southwestern U.S.: Geological Society of America Abstracts with Programs, v. 10, no. 7, p. A327.

Grauch, V.J.S., and Cordell, Lindrith, 1987, Limitations of determining density or magnetic boundaries from the horizontal gradient of gravity or pseudogravity data: Geophysics, v. 52, no. 1, p. 118–121.

Grauch, V.J.S., and Hudson, M.R., 1987, Summary of natural remanent magnetization, magnetic susceptibility, and density measurements from the Lake City caldera area, San Juan Mountains, Colorado: U.S. Geological Survey Open-File Report 87–182, 23 p.

Lee, G.K., McCafferty, A.E., Alminas, H.V., Bankey, Viki, Frishman, David, Knepper, D.H., Jr., Kulik, D.M., Marsh, S.P., Phillips, J.D., Pitkin, J.A., Smith, S.M., Stoeser, D.B., Tysdal, R.G., and Van Gosen, B.S., 2001, Montana geoenvironmental explorer: U.S. Geological Survey Digital Data Series DDS–65.

Lipman, P.W., 1976, Geologic map of the Lake City caldera area, western San Juan Mountains, southwestern Colorado: U.S. Geological Survey Miscellaneous Investigations Series Map I–962, scale 1:48,000.

Luedke, R.G., 1996, Geologic map of the Ophir quadrangle, San Juan, San Miguel, and Dolores Counties, Colorado: U.S. Geological Survey Geologic Quadrangle Map GQ–1760, scale 1:24,000.

Luedke, R.G., and Burbank, W.S., 1975a, Preliminary geologic map of the Handies Peak quadrangle, Colorado: U.S. Geological Survey Open-File Report 75–0431, scale 1:20,000.

Luedke, R.G., and Burbank, W.S., 1975b, Preliminary geologic map of the Howardsville quadrangle, Colorado: U.S. Geological Survey Open-File Report 75–0432, scale 1:20,000.

Luedke, R.G., and Burbank, W.S., 1987, Geologic map of the Handies Peak quadrangle, San Juan, Hinsdale, and Ouray Counties, Colorado: U.S. Geological Survey Geologic Quadrangle Map GQ–1595, scale 1:24,000.

Luedke, R.G., and Burbank, W.S., 2000, Geologic map of the Silverton and Howardsville quadrangles, southwestern Colorado: U.S. Geological Survey Geologic Investigations Map I–2681, scale 1:24,000, 11 p.

Olhoeft, G.R., 1985, Low-frequency electrical properties: Geophysics, v. 50, no. 12, p. 2492–2503.

Phillips, J.D., 1997, Potential-field geophysical software for the PC, version 2.2: U.S. Geological Survey Open-File Report 97–725, 34 p.

Steven, T.A., Lipman, P.W., Hail, W.J., Jr., Barker, Fred, and Luedke, R.G., 1974, Geologic map of the Durango quadrangle, southwestern Colorado: U.S. Geological Survey Miscellaneous Investigations Series Map I–764, scale 1:250,000.

Syberg, F.J.R., 1972, A Fourier method for the regional-residual problem of potential fields: Geophysical Prospecting, v. 20, p. 47–75.

Telford, W.M., Geldart, L.P., Sheriff, R.E., and Keys, D.A., 1976, Applied geophysics: Cambridge, Cambridge University Press.

Wood, Joseph, 1996, The geomorphological characterization of digital elevation models: Leicester, U.K., University of Leicester Department of Geography Ph. D. thesis, 185 p.

Yager, D.B., and Bove, D.J., 2002, Generalized geologic map of part of the upper Animas River watershed and vicinity, Silverton, Colorado: U.S. Geological Survey Miscellaneous Field Studies Map MF–2377, Version 1.0.